

OPTIMIZATION CRITERIA FOR STANDING WAVE  
TRANSVERSE MAGNETIC DEFLECTION CAVITIES

Jacob Haimson  
Massachusetts Institute of Technology\*  
Cambridge, Massachusetts

1. Introduction

An important linear accelerator requirement, in order to demonstrate narrow energy spectra, is the injection of electron bunches of narrow phase spread and negligible inter-bunch current. This can be achieved by r-f transverse modulation and clipping of the beam by an aperture prior to injection into the accelerator waveguide, i.e., chopper operation. By magnetically biasing the beam to one side of the centerline, it is possible to arrange for transmission into the accelerator at a time during each r-f cycle when the radial momentum imparted to the beam by the chopper cavity is passing through zero. The low efficiency of beam utilization normally associated with this type of operation, because of the high ratio of collected to transmitted current, can be considerably improved by combining the transverse chopping action with a suitably phased longitudinal velocity modulating field<sup>1</sup> as obtained from a simple prebunching cavity.

Transverse r-f deflection techniques also enable sub-harmonic bunch selection and injection into linear accelerators which are used as injectors for electron synchrotrons. This is achieved by driving the chopper cavity at the same frequency as the synchrotron r-f system (which is maintained at a precise sub-multiple of the linear accelerator fundamental frequency) and then prebunching the chopped beam at the fundamental frequency prior to injection into the linear accelerator.<sup>2</sup>

2. Microwave Characteristics

A natural choice for the r-f deflector in a linear accelerator injection system is a resonant cavity of small dimensions which can be located in a narrow region adjacent to the gun anode. Preferably, the Q should be high enough to provide adequate deflection sensitivity at a relatively low drive level but not as high as to cause significant beam deflection variations due to small thermal or input power fluctuations.

An electron beam traversing a cavity at right angles to the r-f electric field will tend to undergo a net zero deflection because of the compensating effect of the associated r-f magnetic field.<sup>3</sup> On the other hand, cavities which present purely transverse magnetic fields to the beam offer a simple means of achieving particle deflection. Although the magnetic deflecting force is a function of the electron energy, the net

transverse momentum imparted by the magnetic field (neglecting transit time) will be independent of axial velocity (refer to Equation (3.3)). Thus the beam deflection, and therefore the resulting current transmitted through a clipping aperture, will be less affected by gun voltage ripple than in a comparable system using pure transverse electric deflection.

For beam deflection applications, we are primarily interested in determining

- (a) the location of maximum H field in the cavity,
- (b) the gradient of the field at this location and over a short distance orthogonal to the field lines (i.e., in the transverse deflection path of the beam),
- (c) the wall losses required to establish a given magnetic field strength, and,
- (d) the cavity quality factor Q so that the response of the system to thermal and r-f variations can be assessed.

The location and gradient of the magnetic fields can be determined from the field equations, and a close approximation to the power loss - magnetic field strength relationship can be obtained by considering the ideal conductor peak current surface densities  $J_A$  (as determined from the tangential magnetic fields) and applying these to walls of known surface resistivity ( $R_s$ ) and area (A), i.e.,

$$P_L = \frac{1}{2} R_s \int |J_A|^2 A \quad (2.1)$$

where  $P_L$  is the power loss averaged over the r-f cycle. The line integral of magnetic field, taken around a path which borders on the conducting walls and then extends to infinity, can be equated to the enclosed conduction current; and since  $\vec{J}$  and  $\vec{H}$  are orthogonal, we can write in vector form,

$$\vec{J} = \vec{n} \times \vec{H} \quad (2.2)$$

where  $\vec{n}$  is a unit vector pointing perpendicularly outward from the conducting surface and  $\vec{H}$  is the magnetic field at the surface. Thus, from Equation (2.1) we obtain the basic relationship between the power loss in the walls and the time oscillating magnetic field,

$$P_L = \frac{1}{2} R_s \int |\vec{n} \times \vec{H}|^2 A \quad (2.3)$$

-----

\* Formerly at Varian Associates, Palo Alto, California

The field equations also enable the cavity stored energy (U) to be evaluated from the volume integrals

$$\left( U_E \right)_{\max} = \frac{\epsilon}{2} \iiint_V |E|^2 dV \quad (2.4)$$

or

$$\left( U_H \right)_{\max} = \frac{\mu}{2} \iiint_V |H|^2 dV$$

since the total energy is stored within both the E and H fields, and when one is a maximum, the other is zero.

Finally, from a knowledge of  $P_L$  and U, the quality factor Q can be determined from the well known relationship between stored energy and average power loss per cycle,

$$Q = \frac{\omega U}{P_L} \quad (2.5)$$

### 2.1 General Expressions for the Electric and Magnetic Fields

Two simple cavities which offer the desired type of field distribution are the pill box and sectionalized rectangular waveguide operating in the dominant mode as shown in Figure 1. The cavities have been oriented such that the magnetic fields will be transverse and the electric field parallel to a longitudinally directed beam. Both cavities have magnetic fields surrounding the displacement current represented by the time varying electric field which is a maximum ( $E_0$ ) on axis and falls to zero at the conducting walls. In the case of the pill box cavity, the field components remain constant in both the azimuthal and axial directions; whereas in the rectangular cavity the field components are constant only in the axial direction.

In keeping with convention the rectangular cavity can be considered as a portion of waveguide which normally has a transverse electric field propagating in the p direction but with reflecting planes introduced with  $\lambda_g/2$  separation to satisfy the cavity condition of zero electric field at the walls. Thus for this case and with the mode defined as the number of half wave variations in the x, y, z directions, we obtain

$$TE_{mnp} = TE_{xyz} = TE_{101}$$

The circular cavity mode is described in the azimuthal, radial and axial directions, respectively, as

$$TM_{\ell mn} = TM_{\phi rz} = TM_{010}$$

These conventions will be referred to again when dealing with higher mode fields later in this section.

It has been shown<sup>4,5</sup> that resonant frequencies of the normal-mode fields for a right circular cylinder are expressed in terms of Bessel function roots such that the free space wavelength of the resonant frequency is

$$\lambda_0 = \frac{2}{\sqrt{\left(\frac{\chi_{\ell m}}{\pi a}\right)^2 + \left(\frac{n}{h}\right)^2}} \quad (2.6)$$

For TM modes, the  $\ell mn$  integers are defined by the H field components; and  $\chi_{\ell m}$  is the  $m^{\text{th}}$  root of  $J_{\ell}(k_c a) = 0$ , where  $k_c$  is the propagation constant at the cut-off wavelength. Also, the field equations are defined in Bessel and trigonometric functions such that for the TM components that will be of interest in the following discussion ( $n = 0$ ) we have

$$E_z = E_0 J_{\ell}(k_c r) \{A \sin \ell \phi + B \cos \ell \phi\} \cos \frac{n\pi z}{h} \quad (2.7)$$

$$H_{\phi} = -j \frac{E_0}{\eta} J'_{\ell}(k_c r) \{A \sin \ell \phi + B \cos \ell \phi\} \cos \frac{n\pi z}{h} \quad (2.8)$$

$$H_r = j \frac{E_0}{\eta} \ell \frac{J_{\ell}(k_c r)}{k_c r} \{A \cos \ell \phi - B \sin \ell \phi\} \cos \frac{n\pi z}{h} \quad (2.9)$$

where A and B are constants determined by the mode orientation

$$\begin{cases} \text{For } \ell = 0, & A = 0 & \text{and} & B = 1. \\ \text{For } \ell = 1, & A = 1 & \text{and} & B = 0. \end{cases}$$

and

$$H_z = E_{\phi} = E_r = 0$$

For the  $TE_{mnp}$  modes of a rectangular resonator the propagation constants are given by

$$k_c^2 = \left(\frac{m\pi}{a}\right)^2 + \left(\frac{n\pi}{h}\right)^2 \quad (2.10)$$

and

$$k = \frac{2\pi}{\lambda_0} = \left[ \left(\frac{m\pi}{a}\right)^2 + \left(\frac{n\pi}{h}\right)^2 + \left(\frac{p\pi}{d}\right)^2 \right]^{1/2} \quad (2.11)$$

The associated field components are expressed in trigonometric terms such that for the TE modes of interest ( $n = 0$ ) we have

$$E_y = -j \frac{\omega \mu C}{k_c^2} \left(\frac{m\pi}{a}\right) \sin \frac{m\pi x}{a} \cos \frac{n\pi y}{h} \sin \frac{p\pi z}{d} \quad (2.12)$$

$$H_z = C \cos \frac{m\pi x}{a} \cos \frac{n\pi y}{h} \sin \frac{p\pi z}{d} \quad (2.13)$$

$$H_x = -\frac{C}{k_c} \left(\frac{m\pi}{a}\right) \left(\frac{p\pi}{d}\right) \sin \frac{m\pi x}{a} \cos \frac{n\pi y}{h} \cos \frac{p\pi z}{d} \quad (2.14)$$

and

$$H_y = E_x = E_z = 0$$

## 2.2 Comparison of TM<sub>010</sub> and TE<sub>101</sub> Deflection Field Characteristics

The field distributions for these simple dominant modes (see Figure 1) may be derived by considering the standing wave pattern produced (a) in the cylindrical cavity by inward and outward radially propagated waves and (b) in the rectangular cavity by the reflections between end walls separated by  $d = \lambda_g/2$ .

**2.2.1 Field Distributions.** For the TM<sub>010</sub> mode, substituting  $l = 0$ ,  $m = 1$ , and  $n = 0$  into Equations (2.7), (2.8) and (2.9) gives

$$E_z = E_0 J_0(k_c r) \quad (2.15)$$

$$H_\phi = j \frac{E_0}{\eta} J_1(k_c r) \quad (2.16)$$

as the only field components.  $\eta$  is the intrinsic impedance of the medium ( $\eta = \sqrt{\mu/\epsilon} = 120\pi$  ohm in free space). In order to satisfy the boundary condition in this dominant mode, zero electric field tangential to the wall at  $r = a$ , the first root of the  $J_0$  Bessel function determines the relationship between the propagation constant ( $k_c$ ) and cavity radius ( $a$ ), i.e.,  $k_c a = 2.405$  which leads to the well known resonance requirement

$$\lambda_0 = 2.61a \quad (2.17)$$

The radial variation of  $H_\phi$  is shown plotted in Figure 2. It increases in magnitude from zero on axis to a maximum value ( $H_{\phi M}$ ) at  $r_M = 0.766a$  and then falls to  $0.892H_{\phi M}$  at the cavity wall. This suggests that, for maximum deflection sensitivity, a beam traversal hole or radial slot should be located at radius  $r_M$  as shown by  $e_{Hr}$  in Figure 1(a).

The TE<sub>101</sub> mode field components ( $E_y$ ,  $H_z$ , and  $H_x$ ) are obtained by substituting  $m = 1$ ,  $n = 0$  and  $p = 1$  in Equations (2.10) - (2.14) giving,

$$E_y = -j\omega\mu C \frac{a}{\pi} \sin \frac{\pi x}{a} \sin \frac{\pi z}{d} \quad (2.18)$$

$$H_z = C \cos \frac{\pi x}{a} \sin \frac{\pi z}{d} \quad (2.19)$$

$$H_x = -C \frac{a}{d} \sin \frac{\pi x}{a} \cos \frac{\pi z}{d} \quad (2.20)$$

and

$$\lambda_0 = \frac{2ad}{\sqrt{a^2 + d^2}} \quad (2.21)$$

These equations show that the peak magnetic fields  $H_{Oz}$  and  $H_{Ox}$  occur immediately adjacent to the walls such that, at  $x = 0$  and  $a$ , and  $z = d/2$ ,

$$|H_z| = |H_{Oz}| = C \quad (2.22)$$

and at  $z = 0$  and  $d$ , and  $x = a/2$ ,

$$|H_x| = |H_{Ox}| = \frac{a}{d} |H_{Oz}| \quad (2.23)$$

Equation (2.23) reveals an interesting feature of the TE<sub>101</sub> cavity in that with the exception of a square geometry ( $a = d$ ) the magnetic field strength alongside the center of the long walls will always be more intense than at the center of the short walls. The beam centerline locations, for maximum deflection, corresponding to  $H_{Oz}$  and  $H_{Ox}$  are shown as  $e_{Hz}$  and  $e_{Hx}$ , respectively, in Figure 1(b). In practice, in order to take full advantage of the field maxima adjacent to the wall surface, a small protuberance in the wall, parallel to the surface currents, can be provided to avoid beam collision during that portion of each r-f cycle in which the beam is being deflected toward the wall.

The Figure 2 graphs show magnetic field strength distributions in the directions of beam deflection  $H_\phi(r)$ ,  $H_z(x)$ , and  $H_x(z)$ , plotted against the respective semi-cavity dimensions  $a$ ,  $x/2$ , and  $z/2$  and normalized for equal maxima.

A comparison of more practical value can be obtained by evaluating the cavity wall losses and interpreting them in terms of the maximum magnetic field strength produced by a given level of r-f power coupled in from an external generator. The TE<sub>101</sub> wall loss calculations can be simplified if we modify the magnetic field equations as follows:

From Equations (2.18) and (2.22) the maximum electric field ( $E_0$ ) at  $x = a/2$  and  $z = d/2$  is given by

$$E_0 = -j\omega\mu H_{Oz} \frac{a}{\pi} \therefore E_0 = -j \frac{2a\eta}{\lambda_0} H_{Oz} \quad (2.24)$$

Substituting for  $H_{Oz}$  in Equations (2.19) and (2.20) we obtain

$$H_z = j \frac{\lambda_0}{\eta} \frac{E_0}{2a} \cos \frac{\pi x}{a} \sin \frac{\pi z}{d} \quad (2.25)$$

$$H_x = -j \frac{\lambda}{\eta} \frac{E_o}{2d} \sin \frac{\pi x}{a} \cos \frac{\pi z}{d} \quad (2.26)$$

2.2.2 Evaluation of Wall Losses. For the TM<sub>010</sub> mode using Equations (2.3) and (2.16) the losses in the flat end caps can be written as

$$P_{LE} = 2 \left[ \frac{1}{2} R_s \int_0^a |H_\phi(r)|^2 2\pi r dr \right] \quad (2.27)$$

$$= 2\pi R_s \left( \frac{E_o}{\eta} \right)^2 \int_0^a J_1^2(k_c r) r dr$$

To evaluate this integral, referring to R. V. Churchill "Fourier Series and Boundary Value Problems," 1941, page 162,

$$\int_0^a [J_1(k_c r)]^2 r dr = \frac{a^2}{2} \left\{ [J_1(k_c a)]^2 + [J_2(k_c a)]^2 \right\} - \frac{a}{k_c} J_1(k_c a) J_2(k_c a) \quad (2.28)$$

Also, since

$$\frac{2n}{(k_c a)} J_n(k_c a) = J_{n-1}(k_c a) + J_{n+1}(k_c a),$$

$$\frac{2}{(k_c a)} J_1(k_c a) = J_0(k_c a) + J_2(k_c a) \quad (2.29)$$

But to satisfy the boundary conditions for resonance (see Equations (2.16) and (2.17))  $J_0(k_c a)$  must equal zero, giving

$$J_2(k_c a) = \frac{2}{(k_c a)} J_1(k_c a)$$

Substituting this in Equation (2.28) gives

$$\int_0^a [J_1(k_c r)]^2 r dr = J_1^2(k_c a) \frac{a^2}{2}$$

which when substituted into Equation (2.27) gives the loss in the end caps as

$$P_{LE} = \pi R_s \left( \frac{E_o}{\eta} \right)^2 a^2 J_1^2(k_c a) \quad (2.30)$$

Similarly, for the losses in the circumferential wall,

$$P_{LW} = \frac{1}{2} R_s |H_\phi(a)|^2 2\pi a h$$

$$= \pi R_s \left( \frac{E_o}{\eta} \right)^2 J_1^2(k_c a) a h \quad (2.31)$$

The total losses in the cavity can now be obtained from Equations (2.30) and (2.31) to give

$$P_L = P_{LE} + P_{LW}$$

$$= \pi R_s \left( \frac{E_o}{\eta} \right)^2 J_1^2(k_c a) (a^2 + ah) \quad (2.32)$$

The  $P_{LC}$  and  $P_{LW}$  equations also enable the distribution of losses between the wall and the end caps to be determined. Information of this nature assists in cooling design and in the selection of materials for the control of cavity Q. From the above equations we obtain the simple and useful relationship,

$$\frac{P_{LW}}{P_{LE}} = \frac{h}{a} \quad (2.33)$$

Finally, an expression relating the maximum magnetic field and r-f power for the TM<sub>010</sub> mode can be obtained from Equations (2.16) and (2.32) such that

$$P_L = \pi R_s H_\phi^2 \frac{J_1^2(k_c a)}{J_1^2(k_c r)} (a^2 + ah)$$

and for

$$\frac{r_M}{a} = 0.766, \quad \frac{H_\phi M}{P_L} = \frac{0.40}{a R_s (a + h)} \quad (2.34)$$

A similar procedure can be used for the TE<sub>101</sub> cavity to evaluate the losses in the six internal surfaces. There are equal and opposite charges on the "beam inlet" and "beam outlet" end walls, and the resulting circulating conduction currents have radial flow patterns from the center of these walls (initially) which become parallel in the side walls. From Equation (2.3) and Figure 1(b),

$$P_L = \frac{1}{2} R_s \left[ 2 \int_0^d \int_0^h |H_z|^2 dydz + 2 \int_0^h \int_0^a |H_x|^2 dx dy + 2 \int_0^d \int_0^a (|H_z|^2 + |H_x|^2) dx dz \right]$$

and substituting for  $H_z$  and  $H_x$  from Equations (2.25) and (2.26)

$$P_L = \frac{R_s}{s} \left( \frac{\lambda_o E_o}{\eta} \right)^2 \left[ \frac{ah}{d^2} + \frac{dh}{a^2} + \frac{1}{2} \left( \frac{a}{d} + \frac{d}{a} \right) \right] \quad (2.35)$$

The peak magnetic field can be related to the r-f power by using Equations (2.24) and (2.23) to give

$$\frac{H_{oz}^2}{P_L} = \frac{4d^2}{R_s [2h(a^3 + d^3) + ad(a^2 + d^2)]} \quad (2.36)$$

$$\frac{H_{ox}^2}{P_L} = \frac{4a^2}{R_s [2h(a^3 + d^3) + ad(a^2 + d^2)]} \quad (2.37)$$

**2.2.3 Comparison of Optimized Magnetic Field Maxima.** The  $TM_{010}$  and  $TE_{101}$  magnetic field strengths can now be compared on the practical basis of

- (a) the same "h" dimension along the beam center-line,
- (b) the same r-f power and frequency,
- (c) the same cavity material.

Because the "a" dimension in the  $TM_{010}$  mode is determined by  $\lambda_o$  only, the choice of an "h" dimension allows the maximum value of the deflection factor

$$\left( \frac{H_{\phi M}^2}{P_L} \right)$$

to be uniquely defined. This can be expressed in  $\lambda_o$  normalized dimensions, using Equation (2.34), as

$$\frac{H_{\phi M}^2}{P_L} R_s \lambda_o^2 = \frac{0.40}{\left( \frac{a}{\lambda_o} \right)^2 + \left( \frac{ah}{\lambda_o^2} \right)} \quad (2.38)$$

It should be noted that the surface resistivity  $R_s$  is a function of  $\lambda_o$  and is defined by the material conductivity ( $\sigma$ ) and skin depth ( $\delta$ ) as,

$$R_s = \frac{1}{\sigma \delta} = \sqrt{\frac{\pi f \mu}{\sigma}}$$

For copper  $\sigma = 5.80 \times 10^7$  mhos per meter and  $\mu = 4 \pi \times 10^{-7}$  henrys per meter,

$$\therefore R_s = \frac{4.52 \times 10^{-3}}{\sqrt{\lambda_o}} \text{ ohms} \quad (2.39)$$

For a given "h" dimension in the  $TE_{101}$  mode, however, the "a" and "d" dimensions can be varied over a wide range while still satisfying the Equation (2.21) condition for resonance, i.e.,

$$\frac{a}{\lambda_o} = \frac{1}{2} \sqrt{1 + \left( \frac{a}{d} \right)^2} \quad (2.40)$$

Thus, because the

$$\left( \frac{H_{oz}^2}{P_L} \right)$$

deflection factors will vary accordingly, a meaningful comparison with the uniquely defined  $TM_{010}$  maximum field requires that the  $TE_{101}$  optimum a/d ratio conditions be investigated. Equations (2.35) and (2.36) suggest the existence of an optimum condition because an initial reduction of "a" with respect to "d" will cause  $H_{oz}$  to increase. Too large a reduction, however, will result in reduced fields due to the rapid third order growth of "d".

Letting F equal the right hand side of Equation (2.36) we have

$$\frac{d}{dd} \left( \frac{H_{oz}^2}{P_L} \right) = \frac{\partial F}{\partial d} + \frac{\partial F}{\partial a} \left( \frac{da}{dd} \right)$$

which leads to

$$R_s \frac{d}{dd} \left( \frac{H_{oz}^2}{P_L} \right) =$$

$$\frac{4d^4 \left\{ 2h \left[ -1 + 2 \left( \frac{a}{d} \right)^3 + 3 \left( \frac{a}{d} \right)^5 \right] + a \left[ -1 + 2 \left( \frac{a}{d} \right)^2 + 3 \left( \frac{a}{d} \right)^4 \right] \right\}}{\left[ 2h(a^3 + d^3) + ad(a^2 + d^2) \right]^2}$$

Thus, for a maximum or minimum, setting the numerator of this expression to zero, normalizing to  $\lambda_0$ , and substituting from Equation (2.39) gives

$$\frac{2h}{\lambda_0} \left[ -1 + 2 \left( \frac{a}{d} \right)^3 + 3 \left( \frac{a}{d} \right)^5 \right] = \frac{1}{2} \sqrt{1 + \left( \frac{a}{d} \right)^2} \left[ 1 - 2 \left( \frac{a}{d} \right)^2 - 3 \left( \frac{a}{d} \right)^4 \right] \quad (2.41)$$

The TE<sub>101</sub> mode optimum a/d ratio, obtained from the solution of Equation (2.41), has been plotted against  $h/\lambda_0$  as shown by curve A Figure 3. This curve indicates that the optimum ratio is a slow function of the "h" dimension having a/d ratios of 0.609, 0.626 and 0.632 for  $h/\lambda_0$  values of 0.152, 0.329 and 0.429, respectively. Information of this nature substituted into Equation (2.36) enables the maximum value of

$$\left( \frac{H_{zM}^2}{P_L} \right)$$

to be determined.

The advantage of the optimally dimensioned TE<sub>101</sub> cavity over the other configurations is clearly indicated by comparison of the TM<sub>010</sub> and TE<sub>101</sub> magnetic field maxima optimized as discussed above and listed in Table I for a range of  $h/\lambda_0$  values. Corresponding magnetic field maxima for TE<sub>101</sub> "square" cavities ( $a = d$ ) are also listed in Table I.

A scaled comparison of the magnetic field gradients in the direction of beam deflection,  $H_z(x)$ ,  $H_x(z)$  and  $H_\phi(r)$ , is shown in Figure 4 for  $h/\lambda_0 = 0.329$ . These curves show that, for the same power and frequency, the maximum deflecting magnetic fields for the TM<sub>010</sub> and "square" TE<sub>101</sub> cavities are 75 and 89.5 per cent, respectively, of the optimized TE<sub>101</sub> magnetic field maximum.

Application of the above theory to an actual design problem will clarify the terms and assist the reader in defining the units. For example, let us assume a matched TE<sub>101</sub> copper cavity operating at 2856 MHz with a peak r-f input power of 1 kW. For the optimum a/d ratio and a value of  $h/\lambda_0 = .152$  ( $h = 1.60$  cm) what is the maximum theoretical value of  $H_{zM}$ ?

From Table I and Equation (2.39) we have,

$$H_{zM} = \frac{1.881}{\lambda_0} \left( \frac{10^6 \lambda_0^{1/2}}{4.52} \right)^{1/2} \quad (\lambda_0 = 0.105 \text{ m})$$

$$= 4800 \text{ amp per meter}$$

$$\therefore B = 4800 \times \frac{4\pi}{10^7} \text{ weber per meter}^2$$

$$= 60 \text{ gauss}$$

It should be noted that this value of field is based upon a theoretical loss calculation which, as explained in an earlier section, is related to several assumptions concerning a perfect conductor. In practice the cavity losses are invariably higher, sometimes up to 20 per cent, depending on the matching and fabrication technique; and this causes a reduction of the theoretical field value (~10%). Furthermore, the indicated values of "a", "d" and "h" for a given  $\lambda_0$  are slightly modified in practice to allow for the detuning effects of beam aperture geometry, multipactor suppression treatment, monitoring devices, etc.

Referring again to Table I, reduction of the magnetic field factors with increasing  $h/\lambda_0$  for the same mode should not be regarded as a disadvantage from the overall point of view of beam deflection. As will be shown in a later section, for a given beam energy, the deflection angle is a function of the integrated magnetic field strength experienced by the particle during traversal through the cavity, i.e., a product of the cavity "h" dimension, and the transit time and phase corrected value of magnetic field. Thus a cavity with a large "h" value can be a very efficient deflector even though its

$$\left( \frac{H^2}{P_L} \right)$$

factor is low.

An important practical aspect which may influence the above optimization procedure and which should be given careful consideration is the cavity quality factor Q.

2.2.4 Evaluation and Discussion of Q. A knowledge of the cavity stored energy and loss enables the Q to be determined from Equation (2.5). For the TM<sub>010</sub> mode, using Equations (2.4) and (2.15) the stored energy maxima can be expressed as

$$U_M = \frac{\epsilon}{2} h \int_0^a |E_z|^2 2\pi r dr = \frac{\pi \epsilon}{2} E_0^2 a^2 h J_1^2(ka) \quad (2.42)$$

and substituting Equations (2.42) and (2.32) into (2.5) gives

$$Q = \frac{\pi \mu f}{R_s} \left( \frac{ah}{a+h} \right)$$

Equation (2.17) enables this to be simplified such that

$$QR_s = \frac{453}{\left( \frac{a}{h} + 1 \right)} \text{ MKS} \quad (2.43)$$

which for copper cavities reduces to

$$Q = \frac{10^6 \sqrt{\lambda_o}}{\left(\frac{a}{h} + 1\right)} \text{ MKS} \quad (2.44)$$

The volume integral of the electric field Equation (2.18) gives the TE<sub>101</sub> mode maximum stored energy as

$$U_M = \frac{\epsilon a h d}{8} E_o^2 \quad (2.45)$$

and by combining this with the loss Equation (2.35)

$$QR_s = \frac{\pi \eta}{4} \left[ \frac{2h(a^2 + d^2)^{3/2}}{2h(a^3 + d^3) + ad(a^2 + d^2)} \right] \quad (2.46)$$

The variation of QR<sub>s</sub> with cavity length (h/λ<sub>o</sub>) for the TM<sub>010</sub> mode is shown as curve A in Figure 5 and the TE<sub>101</sub> mode QR<sub>s</sub> has been plotted against (a/λ<sub>o</sub>) in Figure 6 for three specific values of (h/λ<sub>o</sub>). These curves indicate that the TM<sub>010</sub> Q values remain somewhat higher (5 to 10 per cent) than the values for the corresponding optimally dimensioned TE<sub>101</sub> cavities over a range of h/λ<sub>o</sub>. Some typical values have been listed in Table II. For the cavity examples shown in Figure 4, with h/λ<sub>o</sub> = 0.329, the QR<sub>s</sub> curves indicate Q's of ~15,000 for copper surfaces and a frequency of 2856 MHz. Q values of this magnitude are usually undesirable in practice because highly stable frequency and temperature control systems are essential if troublesome variations of the beam deflection are to be avoided. Even if these objections were overcome, a more serious disadvantage becomes apparent when, for pulsed systems, the excitation time of the cavity is considered. For example, the rate of build-up of magnetic (or electric) field strength can be expressed as

$$H_t = H_o \left( 1 - e^{-\omega t / 2Q_L} \right) \quad (2.47)$$

where H<sub>o</sub> is the steady-state field, H<sub>t</sub> is the field strength at time "t" after the start of excitation and Q<sub>L</sub> is the loaded Q of the cavity which equals, Q<sub>o</sub>/2 for matched conditions. If we disregard the mismatch reflection effects, due to the retarded impedance growth during build-up, then with a Q<sub>o</sub> of 15,000 at 2856 MHz the magnetic field will require 2.5 μsec for build-up to the 95 per cent level. At 1300 MHz a cavity of 15,000 Q<sub>o</sub> will take 5.5 μsec to build-up to the 95 per cent level. Figure 7 shows a typical build-up characteristic for the magnetic field strength in a matched cavity of 10,000 Q<sub>o</sub> operating at 2856 MHz. The build-up time (t) at any other frequency and/or Q<sub>o</sub> can be obtained by modifying the time (t<sub>c</sub>) given by the Figure 7 curve as follows:

$$t = t_c \times \frac{Q_o}{10^4} \times \frac{2856}{f(\text{MHz})} \quad (2.48)$$

In general, a build-up time of several microseconds, as for the above Q<sub>o</sub> = 15,000 example, is unacceptable for accelerator injector cavities (choppers and pre-bunchers) which receive pulsed drive power from the same r-f source as the waveguide sections. Optimum accelerator operation often requires the injection of a steady-state beam shortly after commencing application of the r-f pulse power to the waveguide sections. Under these circumstances the chopper and/or pre-buncher cavity build-up times must be less than the waveguide fill-time, e.g., of the order of 0.3 μsec at S-band. The magnetic field build-up problem becomes even more acute for systems that require bunch selection using chopper cavities which operate at a sub-multiple of the accelerator frequency; say 476 MHz to provide 1 bunch in 6 at 2856 MHz. Clearly in this case, with build-up times of the order of 20 μsec, pre-excitation with a long r-f pulse width is required.

A technique commonly used to ensure short transient times of a few tenths of a microsecond at S-band is the aggrandizement of cavity losses such that Q < 2000. This is achieved by constructing the cavity (fully or partially) with stainless steel surfaces or by using lossy coating materials.<sup>6</sup> In addition to lowering Q, the time to reach a given field strength can be reduced by arranging for a cavity coupling factor β > 1. For a given field strength, however, both techniques require increased levels of drive power to supply the additional wall, reflection, and (in some cases) isolation losses.

If the build-up time restriction to Q were removed, the higher more naturally available Q's and magnetic fields could be exploited up to the practical limits of frequency stability. This argues strongly in favor of transverse deflection cavities for CW operation of linear accelerators, narrow band-pass r-f generators, etc., using beam scanning, chopping and/or rotating techniques. Two important advantages (probably vital, with high Q cavities) of this type of operation are (a) the higher degree of system stability inherent with CW operation and (b) the ease of providing a highly sensitive feedback control system.

The manner in which the TE<sub>101</sub> cavity deflecting magnetic field varies with a/λ<sub>o</sub> for a given r-f power level and frequency is shown plotted in Figure 6 for h/λ<sub>o</sub> = 0.152, 0.329 and 0.429. These curves indicate that selection of the optimum (a/d) ratio, rather than the "square" condition (a = d), not only provides the highest magnetic field but also results in a lowering of the Q value.

Because the particle deflection is proportional to the product of magnetic field and a function of the cavity "h" dimension (see Equation (3.12) in a later section), for some applications it will be advantageous to trade-off maximum magnetic field and minimum transit time for larger "h" and Q values.

In brief summary then, optimization of the microwave parameters for a deflection cavity requires

- (a) establishing the largest permissible "h" dimension and Q, (the former is usually dependent upon beam perveance, transit time and system layout restrictions) and
- (b) selecting the most efficient mode and cavity dimensions to provide the best combination of minimum beam aberration and a maximum  $H^2/P_L$  factor.

2.3 Comparison of TM<sub>110</sub> and TE<sub>102</sub> Deflection Field Characteristics

The TM<sub>010</sub> and TE<sub>101</sub> magnetic field gradients in the direction of beam deflection are asymmetrical on either side of the undeflected beam position (H maxima). For the TM<sub>010</sub> mode this is a small effect and if necessary can be easily corrected by a slight radial inward movement of the beam center-line from the  $e_{H\phi}$  position shown in Figure 1(a). With the TE<sub>101</sub> distribution, however, (see Figure 2) large beam cross-sections or deflection angles could result in aberrations that may be unacceptable. Two examples of beam deflecting higher order modes, which offer symmetric H field gradients, are the TM<sub>110</sub> and TE<sub>102</sub> shown in Figure 8. It will be of interest to study the deflection characteristics of these higher order modes and compare them with those of the dominant modes.

2.3.1 Field Distributions. Using the same co-ordinates as in Figure 1, the TM<sub>110</sub> fields of interest can be obtained by substituting  $l = 1, m = 1,$  and  $n = 0$  in Equations (2.7), (2.8) and (2.9) to give

$$E_z = E_o J_1(k_c r) \sin \phi \tag{2.49}$$

$$H_\phi = -j \frac{E_o}{\eta} J_1'(k_c r) \sin \phi \tag{2.50}$$

$$H_r = j \frac{E_o}{\eta} \frac{J_1(k_c r)}{k_c r} \cos \phi \tag{2.51}$$

Also from Equation (2.6) by substituting  $\chi_{lm} = 3.83$  as the first root of  $J_1(k_c a) = 0$  we obtain the resonant condition

$$\lambda_o = 1.64a \tag{2.52}$$

The field equations provide an interesting description of the azimuthal and radial variation of magnetic field which is not immediately apparent from inspection of Figure 8(a). For example,

- (a) When  $\phi = \pi/2$  or  $3\pi/2$ ,  $H_\phi$  has a maximum value ( $H_{\phi M}$ ) at  $r = 0$  and an accompanying but lower secondary peak, of opposite polarity, at  $r = 0.918a$ . Also,  $H_\phi$  falls to zero at  $r = 0.481a$  and is 80.5 per cent of  $H_{\phi M}$  at  $r = a$ .

- (b) When  $\phi = 0$  or  $\pi$ ,  $H_\phi$  is zero for all values of  $r$ , including  $r = 0$ .
- (c)  $H_r$  is zero for all values of  $r$  when  $\phi = \pi/2, 3\pi/2$ .
- (d)  $H_r$  is always zero at  $r = a$ .

These field conditions suggest that, for maximum deflection sensitivity, the beam traversal hole (or slot) should be located at the axis of the cavity as shown in Figure 8(a) by  $e_{H\phi r}$ .

The transverse magnetic field distributions  $H_r(r)$  in the  $\phi = 0$  plane and  $H_\phi(r)$  in the  $\phi = \pi/2$  plane have been plotted in Figure 9. After passing through zero, the  $H_\phi(r)$  reverse polarity distribution follows a pattern similar to the dominant mode with a peak intensity just prior to reaching the cavity wall. The magnetic field reversal points defined by the polar co-ordinates  $r = 0.481a, \phi = \pi/2,$  and  $3\pi/2$ , represent regions of maximum electric field strength with equal and opposite "z" directed vectors of magnitude given by Equations (2.49) and (2.52)

$$E_{zM} = E_o J_1 \left( 2\pi \frac{0.481}{1.64} \right) = 0.582 E_o$$

The Figure 9 curves indicate that the TM<sub>110</sub> mode has excellent aberration - free characteristics over a large central region of the cavity. The maximum variation of transverse magnetic field is less than 5 per cent for beam diameters up to  $0.1 \lambda_o$ . The contour sketches of Figure 9 show polar plots of  $H_\phi$  and  $H_r$ , and the minor distortion of the resultant magnetic field  $|H|$  about  $r = 0$  reveals the aberration - free qualities of the mode. At  $r = 0$  the resultant field can be expressed as

$$|H| = \frac{E_o}{\eta} \left[ (0.5 \sin \phi)^2 + (0.5 \cos \phi)^2 \right]^{1/2} = 0.5 \frac{E_o}{\eta}$$

The TE<sub>102</sub> field components are obtained by substituting  $m = 1, n = 0,$  and  $p = 2$  into Equations (2.10) - (2.14) and using Equation (2.24), giving

$$\lambda_o = \frac{2ad}{\sqrt{4a^2 + d^2}} \tag{2.53}$$

$$E_y = -j \frac{2a\eta}{\lambda_o} H_{oz} \sin \frac{\pi x}{a} \sin \frac{2\pi z}{d} \tag{2.54}$$

$$H_z = H_{oz} \cos \frac{\pi x}{a} \sin \frac{2\pi z}{d} \tag{2.55}$$

$$H_x = -\frac{2a}{d} H_{oz} \sin \frac{\pi x}{a} \cos \frac{2\pi z}{d} \tag{2.56}$$

Unlike the single centrally located TE<sub>101</sub> electric field maxima (Equation (2.18)), Equation (2.54) indicates two equal and oppositely directed electric field vectors

for the TE<sub>102</sub> mode with maxima occurring at  $x = a/2$ ,  $z = d/4$ , and  $x = a/2$ ,  $z = 3d/4$ . (See Figure 8(b).) The displacement currents, associated with these time varying E fields, are surrounded by H fields which produce a pattern in the center of the cavity such that

- (a)  $H_x$  is the only component of magnetic field, and its maximum occurs at  $x = a/2$ ,  $z = d/2$ ,
- (b) the  $H_x$  field distribution is symmetric about this maximum position having a sinusoidal dependence in the "x" direction, a cosinusoidal distribution in the "z" direction, and a constant intensity in the "y" direction.

Thus, for deflection applications, a logical location for beam center-line is as shown by  $e_{HX}$  in Figure 8(b).

The resonance Equation (2.53) indicates that for equal frequencies, and the same "a" dimension as the TE<sub>101</sub> mode, the TE<sub>102</sub> cavity must have twice the "d" dimension. Also, Equations (2.55) and (2.56) show that the peak values of magnetic field are related by

$$|H_{ox}| = \frac{2a}{d} |H_{oz}| \quad (2.57)$$

Because the TE<sub>101</sub> analysis indicated a strong preference for  $H_z$  rather than  $H_x$  fields, and because of the absence of wall losses where the E field goes to zero at  $z = d/2$ , there is cause to believe that this higher order TE<sub>102</sub> mode may possess different optimization characteristics than that of the dominant mode. It is conceivable, for example, that if the symmetry characteristics of the  $H_x(z)$  distribution are essential for a particular application, optimizing the cavity to produce a maximum

$$\left( \frac{H_{xM}^2}{P_L} \right)$$

factor may result in a lower beam deflecting magnetic field than the optimized maximum  $H_z$  field at the walls of the cavity. Questions of this nature can be resolved, as in the previous section, first by analyzing the higher order mode wall losses and then obtaining relationships between power loss and magnetic field strength.

**2.3.2 Evaluation of Wall Losses. For the TM<sub>110</sub> mode,** using Equations (2.3) and the circumferential field component Equation (2.50), the losses in the cylindrical wall can be written

$$P_{LW} = \frac{1}{2} R_s \int_0^{2\pi} \int_0^h \left[ \left( \frac{E_o}{\eta} \right) J_1'(k_c a) \right]^2 a \sin^2 \phi \, dz d\phi$$

$$= \frac{R_s \pi}{2} \left( \frac{E_o}{\eta} \right)^2 ah J_o^2(k_c a) \quad (2.58)$$

Similarly, for the losses in the end caps we have

$$P_{LE} = 2 \frac{R_s}{2} \int_0^{2\pi} \int_0^a \left[ \left( \frac{E_o}{\eta} \right) \left[ J_1'(k_c r) \right]^2 \sin^2 \phi + \left( \frac{E_o}{\eta} \right) \left[ \frac{J_1(k_c r)}{k_c r} \right]^2 \cos^2 \phi \right] r dr d\phi \quad (2.59)$$

Since

$$J_1'(k_c r) = - \frac{J_1(k_c r)}{(k_c r)} + J_o(k_c r) \quad ,$$

(differentiation with respect to  $k_c r$ )

$$P_{LE} = R_s \pi \left( \frac{E_o}{\eta} \right)^2 \int_0^a \left[ \frac{2J_1^2(k_c r)}{(k_c r)^2} - \frac{2J_o(k_c r)J_1(k_c r)}{k_c r} + J_o^2(k_c r) \right] r dr$$

$$\therefore P_{LE} = \frac{R_s \pi}{2} \left( \frac{E_o}{\eta} \right)^2 a^2 J_o^2(k_c a) \quad (2.60)$$

Equations (2.58) and (2.60) reveal that the ratio of wall to end cap losses is the same as for the TM<sub>010</sub> mode, namely,

$$\frac{P_{LW}}{P_{LE}} = \frac{h}{a} \quad (2.61)$$

Therefore, for the same frequency and "h" dimension, the end cap losses for the TM<sub>110</sub> mode will be 59 per cent higher (2.61/1.64) than the TM<sub>010</sub> cavity.

The TM<sub>110</sub> mode total dissipation is obtained from Equations (2.58) and (2.60) such that

$$P_L = P_{LW} + P_{LE} = \frac{R_s \pi}{2} \left( \frac{E_o}{\eta} \right)^2 J_o^2(k_c a) [a^2 + ah] \quad (2.62)$$

(This can be compared against the dominant mode, see Equation (2.32)).

For the TE<sub>102</sub> cavity, because of the symmetric pattern, the surface integrals over the yz and xz walls can be obtained over the half-dimension limits and then

multiplied by four. Using Equation (2.3) and Figure 8 we have

$$P_L = \frac{1}{2} R_s \left[ 4 \int_0^{d/2} \int_0^h \left( H_{oz} \sin \frac{2\pi z}{d} \right)_{x=0}^2 dydz \right. \\ \left. + 2 \int_0^h \int_0^a \left( \frac{2a}{d} H_{oz} \sin \frac{\pi x}{a} \right)_{z=0}^2 dx dy \right] \quad (2.63)$$

$$+ 4 \int_0^{d/2} \int_0^a \left[ \left( H_{oz} \cos \frac{\pi x}{a} \sin \frac{2\pi z}{d} \right)^2 \right. \\ \left. + \left( \frac{2a}{d} H_{oz} \sin \frac{\pi x}{a} \cos \frac{2\pi z}{d} \right)^2 \right] dx dz \\ \therefore P_L = \frac{R_s}{8} \left( \frac{E_o \lambda_o}{\eta} \right)^2 \left[ \frac{dh}{a^2} + \frac{4ah}{d^2} + \frac{1}{2} \left( \frac{d}{a} + \frac{4a}{d} \right) \right] \quad (2.64)$$

Thus, for the case of  $2a = d$ , the losses of the yz, xy and zx walls are proportional to  $2h/a$ ,  $h/a$  and 2, respectively.

The magnetic fields can be related to the power loss by using Equations (2.54)-(2.57) and (2.64) to give

$$\frac{H_{oz}^2}{P_L} = \frac{4d^2}{R_s \left[ 2h(4a^3 + d^3) + ad(4a^2 + d^2) \right]} \quad (2.65)$$

$$\frac{H_{ox}^2}{P_L} = \frac{16a^2}{R_s \left[ 2h(4a^3 + d^3) + ad(4a^2 + d^2) \right]} \quad (2.66)$$

**2.3.3 Optimization and Comparison of the Transverse Magnetic Fields for the TM<sub>110</sub> and TE<sub>102</sub> Modes.** For the TM<sub>110</sub> mode, Equations (2.50) and (2.62) provide a relationship between  $H_\phi$  and power loss such that

$$\frac{H_\phi^2}{P_L} = \frac{2 \left[ J_1'(k_c r) \right]^2 \sin^2 \phi}{R_s \pi J_o^2 (k_c a) \left[ a^2 + ah \right]} \quad (2.67)$$

The maximum and minimum conditions obtained for  $\sin \phi = 1$  from

$$\frac{\partial \left( H_\phi^2 / P_L \right)}{\partial r} = 0$$

are

$$J_o(k_c r) - \frac{J_1(k_c r)}{k_c r} = 0$$

giving a minimum at  $r/a = 0.481$ , and

$$\left[ \frac{2}{(k_c r)^2} - 1 \right] J_1(k_c r) - \frac{J_o(k_c r)}{k_c r} = 0$$

giving a maximum at  $r = 0$  and a relative maximum at  $r/a = 0.918$ . Thus, at  $r = 0$ , the maximum field can be defined in  $\lambda_o$  normalized dimensions as

$$\frac{H_{\phi M}^2}{P_L} R_s \lambda_o^2 = \frac{0.981}{\left( \frac{a}{\lambda_o} \right)^2 + \frac{ah}{\lambda_o^2}} \quad (2.68)$$

For the TE<sub>102</sub> mode, Equation (2.57) indicates that

$$H_{ox} \gtrsim H_{oz} \quad \text{if} \quad 2a \gtrsim d$$

Also, since  $\lambda_c = 2a$  and Equation (2.53) can be rewritten as

$$a = \frac{\lambda_o}{2} \left[ 4 \left( \frac{a}{d} \right)^2 + 1 \right]^{1/2}, \quad (2.69)$$

it is clear that  $a/d < 2$  and  $a/d > 2$  ratios can be chosen to satisfy the resonant condition. Therefore, either the  $H_x$  or the  $H_z$  component of magnetic field can be made to predominate. The optimum dimensions to maximize either of these components can be determined by differentiating Equations (2.65) and (2.66) in a manner similar to the TE<sub>101</sub> example.

To maximize  $H_x$  we have

$$\frac{d}{dd} \left( \frac{H_{ox}^2}{P_L} \right) = \frac{\partial F}{\partial d} + \frac{\partial F}{\partial a} \left( \frac{da}{dd} \right)$$

where  $F =$  right hand side of Equation (2.66), and  $da/dd = -4(a/d)^3$  from Equation (2.53).

Analogous to Equation (2.41), the above provides a maximum value of magnetic field ( $H_{XM}$ ) for a given input power when

$$\frac{2h}{\lambda_0} \left[ 3 + 8\left(\frac{a}{d}\right)^2 - 16\left(\frac{a}{d}\right)^5 \right] = \frac{1}{2} \sqrt{4\left(\frac{a}{d}\right)^2 + 1} \left[ -3 - 8\left(\frac{a}{d}\right)^2 + 16\left(\frac{a}{d}\right)^4 \right] \quad (2.70)$$

The TE<sub>102</sub> mode optimum (a/d) ratios to provide H<sub>x</sub> field maxima for given h/λ<sub>0</sub> values, as obtained from the solution of Equation (2.70), have been plotted as curve B in Figure 3. As before, this proves to have a slowly changing characteristic with (a/d) ratios of 0.875, 0.881 and 0.883 for h/λ<sub>0</sub> values of 0.152, 0.329 and 0.429, respectively.

The condition to maximize H<sub>OZ</sub> can be obtained by differentiating Equation (2.65) which gives

$$\frac{2h}{\lambda_0} \left[ -1 + 8\left(\frac{a}{d}\right)^3 + 48\left(\frac{a}{d}\right)^5 \right] = \frac{1}{2} \sqrt{4\left(\frac{a}{d}\right)^2 + 1} \left[ 1 - 8\left(\frac{a}{d}\right)^2 - 48\left(\frac{a}{d}\right)^4 \right] \quad (2.71)$$

The solution of this equation is plotted as curve C in Figure 3; and optimum (a/d) ratios of 0.315, 0.337 and 0.344 are obtained for h/λ<sub>0</sub> values of 0.152, 0.329 and 0.429, respectively.

The maximum deflection fields, H<sub>ZM</sub> and H<sub>xM</sub>, as obtained by substituting the optimum (a/d) ratios into Equations (2.65) and (2.66) are shown listed in Table III. The corresponding magnetic field maxima for the TM<sub>110</sub> mode and for the 2a = d, TE<sub>102</sub> mode are also listed for comparison purposes.

An interesting feature of the Table III data is that, unlike the dominant mode examples, the circular cavity is superior to the rectangular cavity in attaining a maximum magnetic field for a given power loss. Also, for the TE<sub>102</sub> mode it can be noted that the H<sub>x</sub> field combines the advantages of both the higher order and dominant modes; namely, a symmetric distribution about the beam center-line and the capability of being optimized to provide the higher of the two transverse field maxima.

The interchange of predominance between the TE<sub>102</sub> magnetic field components H<sub>Ox</sub> and H<sub>Oz</sub> with increasing (a/d) ratios is shown plotted against a/λ<sub>0</sub> in Figure 10 for h/λ<sub>0</sub> = 0.152. These curves show that the magnetic field strengths at the cross-over point a/λ<sub>0</sub> = 0.707 (2a = d) are ~35 per cent lower than the comparable "square" (a = d) TE<sub>101</sub> case. (Refer to Table I.) The maximum magnetic field, H<sub>ZM</sub>, which is located at the

zy walls (see inset sketch Figure 10), is critically dependent on the "a" dimension because of its close proximity to cut-off for the optimum (a/d) ratio. In contrast, the H<sub>x</sub> component has a relatively broad optimum and a 5 to 10 per cent higher maximum value than H<sub>ZM</sub> for the range of h/λ<sub>0</sub> indicated in Table III.

It can be shown that the TE<sub>102</sub> characteristics are reproduced exactly by the orthogonal mode, TE<sub>201</sub>. Repeating the optimization procedures with the substitutions m = 2, n = 0, and p = 1 in the field equations merely results in an interchange of roles between the H<sub>Ox</sub> and H<sub>Oz</sub> field components. The most favorable magnetic field still occurs at the cavity center and is directed parallel to the short side walls, i. e., the direction of beam deflection remains parallel to the long walls.

A scaled comparison of the TM<sub>110</sub> and TE<sub>102</sub> optimum magnetic field gradients in the direction of beam deflections, H<sub>φ</sub>(r), H<sub>x</sub>(z) and H<sub>z</sub>(x) is shown in Figure 11 for h/λ<sub>0</sub> = 0.329. It should be noted that only half of the H<sub>φ</sub>(r) and H<sub>x</sub>(z) distributions are shown and these fields are symmetric about the maximum intensity points located at their respective origins, r = 0 and z = d/2. On the other hand, the H<sub>z</sub>(x) distribution is shown plotted from the maximum intensity point at one wall (x = 0), through the minimum, to H<sub>ZM</sub> at the other wall (x = a). The distributions are plotted with respect to λ<sub>0</sub> so that field gradients across the beam, for the various modes, can be compared with convenience. This subject is discussed in section 2.4.

As before, the choice of mode and cavity dimension, for a particular application, can be strongly influenced by the Q value which for these higher orders (comparing equal frequencies) is usually greater than the related dominant mode.

2.3.4 Evaluation of Stored Energy and Q for the TM<sub>110</sub> and TE<sub>102</sub> Modes. For the TM<sub>110</sub> mode, using Equations (2.4) and (2.49), the stored energy can be expressed as

$$U = \frac{\epsilon}{2} \int_0^a \int_0^{2\pi} \int_0^h E_0^2 J_1^2(k_c r) \sin^2 \phi \, r \, dz \, d\phi \, dr \quad (2.72)$$

$$= \frac{\epsilon}{2} E_0^2 h \pi \int_0^a r J_1^2(k_c r) \, dr$$

$$\therefore U = \frac{\pi \epsilon}{4} E_0^2 a^2 h J_0^2(k_c a) \quad (2.73)$$

A comparison with Equation (2.42) indicates that the dominant mode has 11 per cent less stored energy at the same frequency and for the same "h" dimension.

Substituting Equations (2.73) and (2.62) into (2.5) gives

$$Q = \frac{\pi f \epsilon h a \eta^2}{R_s (a+h)}$$

and using Equation (2.52)

$$QR_s = \frac{\pi \eta}{1.64 \left(\frac{a}{h} + 1\right)} = \frac{722}{\left(\frac{a}{h} + 1\right)} \quad (2.74)$$

For the  $TE_{102}$  mode, because the electric field Equation (2.54) is the same as for the dominant mode, the stored energy expression remains the same as Equation (2.45) i.e.,

$$U = \frac{\epsilon a h d}{8} E_o^2$$

(The actual numerical values will, of course, be different.) Combining this with the power loss Equation (2.64) and substituting in Equation (2.5), we obtain

$$Q = \frac{4\pi a h d \eta}{R_s \lambda_o^3 \left[ \frac{d}{a^2} (a + 2h) + \frac{4a}{d^2} (d + 2h) \right]}$$

Substituting for  $\lambda_o$  from Equation (2.53) gives

$$QR_s = \frac{\pi \eta}{4} \left[ \frac{2h(4a^2 + d^2)^{3/2}}{2h(4a^3 + d^3) + ad(4a^2 + d^2)} \right] \quad (2.75)$$

The dependence of  $QR_s$  on cavity length ( $h/\lambda_o$ ) for the  $TM_{110}$  mode is plotted as curve B in Figure 5. Comparison with curve A shows an increase in gain of Q over the dominant mode for increasing values of "h". A graph of  $QR_s$  versus  $a/\lambda_o$  for the  $TE_{102}$  mode and  $h/\lambda_o = 0.152$  is shown in Figure 10 and indicates a 10 to 20 per cent increase over the  $TE_{101}$  mode. (See Figure 6.)

Theoretical Q values for the  $TM_{110}$  and optimized  $TE_{102}$  cavities are listed in Table IV and, for the same  $h/\lambda_o$ , can be compared directly with Table II values for the  $TM_{010}$  and  $TE_{101}$  modes.

#### 2.4 Comparison of Beam Aberration Effects

Because of the finite size of the beam, it can be expected that several factors will contribute to beam aberrations. Major among these are

- (a) the magnetic field gradient across the beam in the direction of deflection, (This will be both time and space dependent and as a consequence will vary with entry phase angle, degree of deflection and transit time.)

- (b) the magnetic field gradient across the beam at right angles to the direction of deflection, (In every case this gradient is less than that of the optimized maximum deflecting magnetic field, e.g., refer Figure 4,  $H_z(x)$ ,  $H_x(z)$ , Figure 9,  $H_\phi(r)$ ,  $H_r(r)$ , etc.)
- (c) non-cancellation of the velocity modulation effects of the longitudinal electric fields, especially for the peripheral particles, and
- (d) fringe and leakage fields due to large or incorrectly shaped beam apertures.

For a given beam diameter, all of these factors are strongly related to the choice of mode and, more particularly, to whether or not the deflecting field is symmetric about the beam center-line.

Table V compares the deflecting magnetic field gradients across increasing beam diameters for the optimized conditions of the previously discussed modes and  $h/\lambda_o = 0.329$ . The results are listed as percentage bins of the appropriate maxima to cover the asymmetric distribution cases, and they disregard the small transverse displacement of the beam during transit. In general the data bears out an intuitive observation that, for equal power and frequency and a given ratio of beam diameter to free space wavelength, the higher the optimum value of deflecting magnetic field, the worse the gradient across the beam.

Avoidance of an off-set beam center-line, with respect to the peak field position, enables the three symmetric distributions of Table V to exhibit low aberration characteristics. For beam diameters up to  $0.15 \lambda_o$  the maximum H gradients are less than 9 per cent and as the gradients at right angles to the beam deflection are even lower, it is seen that the  $TM_{010}$ ,  $TM_{110}$  and  $H_x$  optimized  $TE_{102}$  modes are more favorably suited for the deflection of large beams than the  $TE_{101}$  mode. On the other hand, the high

$$\left( \frac{H_{zM}^2}{P_L} \right)$$

deflection factor of the  $H_z$  optimized  $TE_{101}$  mode makes this a natural choice for small beam applications and when r-f power is at a premium. Selection of 1 bunch in 6 for linear accelerator injection into synchrotrons is an excellent example in this category because the chopper cavity operates at 1/6 of the fundamental frequency, i.e., the ratio of beam diameter to the chopper free space wavelength is reduced by a factor of 6.

As discussed in the introduction, deflection compensation, due to crossed E and H fields, is avoided by arranging for the beam to traverse the cavity parallel to the electric field. For this condition, however, a second order deflection effect is introduced by the velocity modulating action of the longitudinal electric field. For example, consider the higher order modes

which provide symmetric field distributions about the beam center-line. When the particle reaches the center of the cavity, the deflecting magnetic field is a maximum, and the equal and oppositely directed E fields on either side of the beam fall to zero. On entering the cavity, however, the velocity of peripheral particles on one side of the center-line will be reduced and on the other side increased. When the slower particles reach the center of the cavity, they will have been deflected away from the center-line more than the faster particles will have been bent towards it. At this point the E fields will reverse; and because the slower particles are closer to the region of E field maximum, they will experience more voltage gain than that required to compensate for their initial loss in velocity. Also, these particles will be entering regions of lower magnetic field than the faster particles, which will be continuing to deflect toward regions of higher H field and lower (under-compensating) E fields. This process will result in a cross-sectional focusing force in the plane of deflection.

The above description applies for particles, in azimuthal positions along the central plane of deflection, which pass through the cavity center when the deflecting magnetic field is at a maximum. The process will change (a) for particles in other azimuthal positions, owing to additional cross-product terms giving rise to different velocity modulation and transverse forces, and (b) with time during the r-f cycle. (This is discussed further in Section 3.3.)

Beam aberrations during deflection can also be produced by fringe and leakage fields associated with the beam apertures in the cavity. With some higher order modes, for example, the use of beam apertures which have large dimensions at right angles to the paths of the end-cap currents can cause transverse electric field patterns to be established across the aperture tending to counteract beam deflection.

Bead perturbation techniques are commonly used to evaluate the deflection and aberration characteristics of a given cavity design. Although outside the scope of this report, some bead perturbation data relating to a TE<sub>102</sub> mode are shown in Figure 12. The voltage transmission characteristics as obtained when a ceramic bead is drawn down the long axis is shown in Figure 12(a). The result of a metal bead drawn through the cavity parallel to the beam axis at different locations within the aperture is shown in Figure 12(b). The reduced perturbation effect due to compensation of the H and E fields can be clearly noted for the A and C positions.

An analysis of the effects of aberration at the point of application of the deflected beam must of course take into account space charge forces and intervening parameters such as type of focusing, length of drift space, amount of beam biasing (if any), etc., and will depend, therefore, on the particular system layout.

### 2.5 Comparison of Electric Field Maxima

Apart from deflection applications, the transverse magnetic field cavities can also be used for r-f signal extraction, e.g., electron beam position monitoring, r-f power generation, etc. A comparison of the optimized E field maxima for various modes is given in Table VI. If we assume the factor

$$(\lambda_o / \eta) \sqrt{R_s / P_L}$$

is a constant, then for  $h/\lambda_o = 0.152$  the  $E_{zM}$  ratio of TM<sub>110</sub> to the TM<sub>010</sub> is equal to 0.705. Also, because the TM<sub>110</sub> mode  $E_{zM} = 0.582 E_o$  (from Section 2.3.1.) and the TM<sub>010</sub> mode  $E_{zM} = E_o$ , the  $E_o$  ratio of TM<sub>110</sub> to TM<sub>010</sub> is equal to 1.21. A scaled comparison of the radial variation of  $E_z$  for these two modes is shown plotted in Figure 13. Location of beam apertures in the end walls of these cavities, at the peak field positions, will of course modify these ideal distributions and should be taken into account in beam interaction analysis.

### 3. Beam Deflection and Aberration Calculations

For the purpose of consistency, the following analysis will use the same co-ordinates as in Section 2. Considering the TM<sub>110</sub> cavity, for example, the initial beam path lies along the "z" axis and the  $H_\phi$  field will cause deflection in the "r" direction as shown in Figure 14. On this basis, we wish to determine the transverse displacement and momentum of a particle at  $z = h$ , i.e., the plane of departure. A knowledge of the axial velocity ( $\beta_e c$ ) and drift length (S) then enables the total deflection ( $\chi$ ) to be computed.

#### 3.1 Beam Deflection Derived from Simplified Equation of Motion

From Figure 14, the transverse momentum ( $p_\perp$ ) gained during a small interval of time may be written

$$\Delta p_\perp = \beta_e c e \mu H_\phi(t) \Delta t \quad (3.1)$$

where  $H_\phi$  is the effective transverse magnetic field experienced by an axial particle while traversing a distance,

$$\Delta z = \beta_e c \Delta t \quad (3.2)$$

$$\begin{aligned} \therefore m \dot{r} &= e \mu \int_0^h H_{\phi M} \sin \left( \theta_o + \frac{2\pi z}{\beta_e \lambda_o} \right) dz \\ &= e \mu h H_{\phi M}^T \end{aligned} \quad (3.3)$$

where

T = transit time correction factor

$$= \frac{1}{\theta_T} \left[ \cos \theta_o - \cos(\theta_o + \theta_T) \right], \quad (3.4)$$

$\theta_o$  is the phase of the magnetic field corresponding to the particle arrival time at the entry plane  $z = 0$  (for a convention of peak magnetic field at  $\theta = \pi/2$  when the particle is at the center of the cavity), and  $\theta_T$  is the transit angle given by

$$\theta_T = 2\pi \frac{h}{\beta \lambda_{e o}} \quad (3.5)$$

The reduction factor applied to  $H_{\phi M}$  due to the transit time correction will be minimized by optimum selection of the entry phase angle such that

$$\theta_o = \frac{\pi}{2} - \frac{\theta_T}{2} \quad (3.6)$$

Substituting this into Equation (3.4) and using Equation (3.5)

$$T_M = \frac{2}{\theta_T} \sin \frac{\theta_T}{2}$$

$$\therefore T_M = \frac{\beta \lambda_{e o}}{\pi h} \sin \frac{\pi h}{\beta \lambda_{e o}} \quad (3.7)$$

The transverse velocity can now be expressed in terms of the most favorable magnetic field condition by using Equations (3.3) and (3.7) giving

$$\dot{r} = \left( \frac{\mu e}{\gamma m_o} \right) \frac{\beta \lambda_{e o}}{\pi} H_{\phi M} \sin \frac{\pi h}{\beta \lambda_{e o}} \quad (3.8)$$

Defining the deflection angle ( $\alpha$ ) as

$$\tan \alpha = \frac{\dot{r}}{\beta c}, \quad (3.9)$$

$$\tan \alpha = \left( \frac{e}{m_o} \right) \frac{\mu \lambda_{e o}}{\gamma \pi c} H_{\phi M} \sin \frac{\pi h}{\beta \lambda_{e o}}$$

which in the MKS system may be reduced to

$$\tan \alpha = 2.35 \times 10^{-4} \frac{\lambda_{e o}}{\gamma} H_{\phi M} \sin \frac{\pi h}{\beta \lambda_{e o}} \quad (3.10)$$

Also, from Figure 14, the deflection angle can be expressed as

$$\tan \alpha = \frac{\chi}{\left( S + \frac{h}{2} \right)} \quad (3.11)$$

$$\therefore \chi = 2.35 \times 10^{-4} \frac{\lambda_{e o}}{\gamma} \left( S + \frac{h}{2} \right) H_{\phi M} \sin \frac{\pi h}{\beta \lambda_{e o}} \quad (3.12)$$

For a given system geometry and a knowledge of  $H_{\phi M}$ , as obtained from Section 2, Equation (3.12) provides a convenient and reasonably accurate method of determining the beam deflection.

**3.1.1 Generalized Beam Deflection Equations in Terms of Drive Power and Cavity Dimensions.** Equation (3.12) may be expressed in the more general terms of r-f power and cavity dimensions by making the appropriate substitution for the magnetic field strength.

For the TM<sub>110</sub> mode, substituting from Equations (2.68) and (2.52) gives

$$\chi = 2.98 \times 10^{-4} \left( \frac{S + \frac{h}{2}}{\gamma} \right) \left[ \frac{P_L}{R_s \left( 0.61 + \frac{h}{\lambda_o} \right)} \right]^{1/2} \sin \frac{\pi h}{\beta \lambda_{e o}} \quad (3.13)$$

For a copper cavity,

$$R_s = (4.52 \times 10^{-3}) / \sqrt{\lambda_o},$$

and Equation (3.13) may be written

$$\chi = 44.3 \times 10^{-4} \left( \frac{S + \frac{h}{2}}{\gamma} \right) \left[ \frac{P_L \lambda_o^{1/2}}{0.61 + \frac{h}{\lambda_o}} \right]^{1/2} \sin \frac{\pi h}{\beta \lambda_{e o}} \quad (3.14)$$

For a frequency of 2856 MHz and assuming a practical Q 10 per cent lower than the theoretical value, Equation (3.14) becomes,

$$\chi = 7.75 \times 10^{-4} \left( \frac{S + \frac{h}{2}}{\gamma} \right) \left[ \frac{P_L}{0.064 + h} \right]^{1/2} \times \quad (3.15)$$

$$\sin \frac{29.9h}{\beta e} \text{ meter}$$

For the optimized H<sub>ZM</sub> TE<sub>101</sub> mode, substituting from Table I for  $h/\lambda_o = 0.152$  enables Equation (3.12) to be written

$$\chi = 2.35 \times 10^{-4} \left( \frac{S + \frac{h}{2}}{\gamma} \right) 1.881 \left( \frac{P_L}{R_S} \right)^{1/2} \sin \frac{0.479}{\beta_e} \quad (3.16)$$

which for a copper cavity becomes

$$\chi = 65.7 \times 10^{-4} \left( \frac{S + \frac{h}{2}}{\gamma} \right) \left( P_L \lambda_o \right)^{1/2} \sin \frac{0.479}{\beta_e} \quad (3.17)$$

At 2856 MHz, assuming a 10 per cent reduction in the theoretical value of Q, for h = 0.016m Equation (3.17) becomes,

$$\chi = 35.5 \times 10^{-4} \left( \frac{S + 0.008}{\gamma} \right) P_L^{1/2} \sin \frac{0.479}{\beta_e} \text{ meter} \quad (3.18)$$

For the optimized  $H_{xM}$  TE<sub>102</sub> mode and a value of  $h/\lambda_o = 0.152$ , substituting from Table III enables Equation (3.12) for a copper cavity to be written

$$\chi = 49.9 \times 10^{-4} \left( \frac{S + \frac{h}{2}}{\gamma} \right) \left( P_L \lambda_o \right)^{1/2} \sin \frac{0.479}{\beta_e} \quad (3.19)$$

For 2856 MHz and a 10 per cent reduction of theoretical Q, Equation (3.19) becomes

$$\chi = 26.9 \times 10^{-4} \left( \frac{S + 0.008}{\gamma} \right) P_L^{1/2} \sin \frac{0.479}{\beta_e} \quad (3.20)$$

For other values of  $h/\lambda_o$ , the  $H_{zM}$  or  $H_{xM}$  substitutions can be interpolated from the Table I or Table III data.

Graphs of beam deflection versus drift distance for a 2856 MHz, TM<sub>110</sub> copper cavity (Equation (3.15)) having  $h/\lambda_o$  values of 0.152 and 0.329 are shown plotted in Figure 15 for electron energies of 70 and 150 keV and a peak input r-f power level of 4 kW. It can be noted that the 70 and 150 keV beams have equal transverse displacements, at S = 14 cm, for cavities with  $h/\lambda_o$  of 0.152 and 0.329, respectively. Furthermore, unlike the 150 keV beam, the deflection of the 70 keV beam will actually be reduced when a cavity having the larger  $h/\lambda_o$  value is employed. These effects are due to an inter-relation between the particle transit time and transverse momentum at emergence from the cavity.

The data indicates that the Figure 15,  $h/\lambda_o$  values will not produce maximum deflection for a given r-f input power and that an optimization procedure should

be applied to the overall trajectory in order to obtain the ideal value of  $h/\lambda_o$  for a given beam energy and drift length.

3.1.2 Optimization of the "h" Dimension to Produce Maximum Deflection for a Given Drift Length and Beam Energy. For the TM<sub>110</sub> mode, substituting for  $H_{\phi M}$  from Equation (2.68) into Equation (3.12), differentiating with respect to "h", and equating to zero, we obtain

$$\frac{1}{2} \left[ \left( \frac{a}{\lambda_o} \right)^2 + \frac{ah}{\lambda_o^2} \right] \sin \frac{\pi h}{\beta_e \lambda_o} + \left( S + \frac{h}{2} \right) \left[ - \frac{a}{2\lambda_o^2} \sin \frac{\pi h}{\beta_e \lambda_o} + \left( \frac{a}{\lambda_o} \right)^2 + \frac{ah}{\lambda_o^2} \right] \frac{\pi}{\beta_e \lambda_o} \cos \frac{\pi h}{\beta_e \lambda_o} = 0$$

giving

$$S = - \frac{h}{2} - \frac{(a + h)}{-1 + \frac{2\pi}{\beta_e \lambda_o} (a + h) \cotan \frac{\pi h}{\beta_e \lambda_o}} \quad (3.21)$$

The optimum "h" dimension to provide maximum deflection for a given input r-f power may be determined from the solution of Equation (3.21) for a given drift length, beam energy and operating frequency. As  $\lambda_o = 1.64a$ , for the TM<sub>110</sub> mode, at a frequency of 2856 MHz Equation (3.21) may be reduced to

$$S = - \frac{h}{2} - \frac{0.064 + h}{-1 + \frac{59.8}{\beta_e} (0.064 + h) \cotan \frac{29.9h}{\beta_e}} \quad (3.22)$$

For the TE<sub>102</sub> mode, the deflection Equation (3.12) may be written

$$\chi = \left( S + \frac{h}{2} \right) \frac{\mu_e}{\gamma m_o} \frac{\lambda_o}{\pi c} H_{xM} \sin \frac{\pi h}{\beta_e \lambda_o} \quad (3.23)$$

Unlike the TM<sub>110</sub> mode, however, this relationship involves two dependent variables, "d" and "h", and  $\chi$  will be a maximum if

$$\frac{\partial \chi}{\partial h} = 0 \quad \text{and} \quad \frac{\partial \chi}{\partial d} = 0$$

But,

$$\frac{\partial \chi}{\partial d} = 0 \implies \frac{\partial H_{xM}}{\partial d} = 0 \quad (3.24)$$

As before, Equation (3.24) is satisfied by Equation (2.70) which may be re-written as

$$h = \frac{a}{2} \left[ \frac{-3 - 8\left(\frac{a}{d}\right)^2 + 16\left(\frac{a}{d}\right)^4}{3 + 8\left(\frac{a}{d}\right)^2 - 16\left(\frac{a}{d}\right)^5} \right] \quad (3.25)$$

where "a" is a function of "d" given by Equation (2.53).

Also, for  $\partial\chi/\partial h = 0$ , from Equation (3.23) we obtain

$$\begin{aligned} \frac{1}{2} H_{xM} \sin \frac{\pi h}{\beta_e \lambda_o} + \frac{\pi}{\beta_e \lambda_o} \left( S + \frac{h}{2} \right) H_{xM} \cos \frac{\pi h}{\beta_e \lambda_o} \\ + \left( S + \frac{h}{2} \right) \sin \frac{\pi h}{\beta_e \lambda_o} \frac{\partial H_{xM}}{\partial h} = 0 \end{aligned} \quad (3.26)$$

and differentiating Equation (2.66) with respect to "h" gives

$$\begin{aligned} \frac{\partial H_{xM}}{\partial h} = \frac{1}{2H_{xM}} \left( \frac{P}{R_s} \right) 32a^2 (4a^3 + d^3) \\ \left( \frac{-1}{\left[ 2h(4a^3 + d^3) + ad(4a^2 + d^2) \right]^2} \right) \end{aligned} \quad (3.27)$$

Substituting for  $\partial H_{xM}/\partial h$  from Equation (3.27) into Equation (3.26) and re-arranging we obtain

$$s = -\frac{h}{2} \frac{\frac{1}{2} [2h(4a^3 + d^3) + ad(4a^2 + d^2)] \sin \frac{\pi h}{\beta_e \lambda_o}}{\frac{\pi}{\beta_e \lambda_o} [2h(4a^3 + d^3) + ad(4a^2 + d^2)] \cos \frac{\pi h}{\beta_e \lambda_o} - (4a^3 + d^3) \sin \frac{\pi h}{\beta_e \lambda_o}} \quad (3.28)$$

The solution of Equation (3.28), after substituting for "h" from Equation (3.25), provides the optimum relationship between the drift length and the TE<sub>102</sub> cavity "h" dimension to produce maximum deflection for a given beam energy and system frequency.

For the TE<sub>101</sub> mode, a similar procedure as that used for the TE<sub>102</sub> case yields

$$h = \frac{a}{2} \left[ \frac{1 - 2\left(\frac{a}{d}\right)^2 - 3\left(\frac{a}{d}\right)^4}{-1 + 2\left(\frac{a}{d}\right)^3 + 3\left(\frac{a}{d}\right)^5} \right] \quad (3.29)$$

and

$$s = -\frac{h}{2} \frac{\frac{1}{2} [2h(a^3 + d^3) + ad(a^2 + d^2)] \sin \frac{\pi h}{\beta_e \lambda_o}}{-(a^3 + d^3) \sin \frac{\pi h}{\beta_e \lambda_o} + \frac{\pi}{\beta_e \lambda_o} [2h(a^3 + d^3) + ad(a^2 + d^2)] \cos \frac{\pi h}{\beta_e \lambda_o}} \quad (3.30)$$

the combined solution of which provides the optimum relationship between drift length and TE<sub>101</sub> cavity "h" dimension.

Solutions of the TE<sub>101</sub> Equations (3.29) and (3.30), the TM<sub>110</sub> Equation (3.22) and the TE<sub>102</sub> Equations (3.25) and (3.28) are shown in Figure 16 for an operational frequency of 2856 MHz. Optimum "h" values have been plotted against drift distance for  $\beta_e$  values of 0.4759, 0.5584, and 0.6343, corresponding to beam energies of 70, 105 and 150 keV, respectively. As an example, for the TM<sub>110</sub> mode and a given input r-f power, maximum deflection of 70, 105 and 150 keV beams will be produced at the end of a 20 cm drift length with cavity "h" values of 2.42, 2.82, and 3.20 cm, respectively.

The Figure 16 graphs reveal that the optimum "h" values extend over a broad range, dependent on the beam energy and drift space length. For design purposes, therefore, it is of interest to determine how the beam deflection is affected by departure from these optima, due to a mechanical or Q value restriction or a major change in beam energy. This is indicated by the graphs of beam deflection versus cavity "h" dimension shown plotted in Figure 17 for the above mentioned beam energies and a fixed drift distance of 20 cm. These examples were computed for 2856 MHz copper cavities having 90 per cent of the theoretical Q value and an input r-f power level of 4 kW. The deflection reducing influence of the beam apertures on the cavity fields was not taken into account.

The Figure 17 curves also depict an aspect which is of particular value in certain beam deflection applications: namely, that for a given mode and a given value of "h", the beam energy can be varied as much as two to one while the beam deflection remains essentially constant, e.g. in the TM<sub>110</sub> mode, for S = 20 cm and h = 3.28 cm,  $\chi$  changes by only  $\pm 2-1/2$  per cent as the beam energy is varied over the range 70 to 150 keV.

### 3.2 Equations of Motion Including the Effects of Magnetic and Electric Field Variation Along the Deflection Trajectory of the Particle

The simplified preceding analysis disregarded the spatial variation of the deflecting magnetic field experienced by the particle during divergence from trajectories initially directed perpendicular to the region of maximum deflecting magnetic field. With the transit times normally encountered in practical devices, the correction to the magnitude of the deflection due to this spatial variation is of little consequence. On the other

hand, if it is necessary to investigate changes in beam cross-section during deflection, allowance must be made for the spatial and temporal variations of all the field components. This is particularly the case for beams which have relatively large cross-sections with respect to the cavity free space wavelength.

Qualitative contributions to beam aberration, due to the electric fields, have been discussed in Section 2.4. Apart from the longitudinal electric field effects, however, all of the particles undergoing deflection will experience additional velocity modulation contributions due to forces which arise from the transverse velocity cross products. Also, for particles which are remote from the centrally located transverse plane passing through the region of peak deflecting magnetic field, the cross product velocity modulation effects will be accompanied by focusing (and defocusing) forces, i.e., the orthogonal magnetic field components give rise to orthogonal transverse displacements as well as velocity modulating forces.

**3.2.1 Cylindrical and Rectangular Cartesian Coordinate Systems.** For a single electron ( $e = -q$ ) traveling at velocity  $\underline{v}$  through electric ( $\underline{E}$ ) and magnetic fields ( $\underline{B} = \mu \underline{H}$ ) the equation of motion may be written

$$\frac{d}{dt} (\gamma m_0 \underline{v}) = e [\underline{E} + \underline{v} \times \mu \underline{H}] \quad (3.31)$$

In cylindrical co-ordinates,

$$\begin{aligned} \underline{v} \times \mu \underline{H} &= \mu \begin{vmatrix} \underline{r} & \underline{\phi} & \underline{z} \\ v_r & v_\phi & v_z \\ H_r & H_\phi & H_z \end{vmatrix} \\ &= \mu \underline{r} (v_\phi H_z - v_z H_\phi) - \mu \underline{\phi} (v_r H_z - v_z H_r) \\ &\quad + \mu \underline{z} (v_r H_\phi - v_\phi H_r) \end{aligned} \quad (3.32)$$

therefore

$$\begin{aligned} e [\underline{E} + \underline{v} \times \mu \underline{H}] &= \underline{r} e (E_r + \mu v_\phi H_z - \mu v_z H_\phi) \\ &\quad + \underline{\phi} e (E_\phi - \mu v_r H_z + \mu v_z H_r) \\ &\quad + \underline{z} e (E_z + \mu v_r H_\phi - \mu v_\phi H_r) \end{aligned}$$

For the left hand side of Equation (3.31), because  $\gamma$  is a variable

$$\frac{d}{dt} (\gamma m_0 \underline{v}) = \underline{v} \frac{d}{dt} (\gamma m_0) + \gamma m_0 \frac{d\underline{v}}{dt} \quad (3.33)$$

and since

$$\underline{v} = \underline{r} v_r + \underline{\phi} v_\phi + \underline{z} v_z$$

we obtain

$$\begin{aligned} \frac{d}{dt} (\gamma m_0 \underline{v}) &= \underline{r} \left[ v_r \frac{d}{dt} (\gamma m_0) + \gamma m_0 \frac{dv_r}{dt} - \gamma m_0 v_\phi \frac{d\phi}{dt} \right] \\ &\quad + \underline{\phi} \left[ v_\phi \frac{d}{dt} (\gamma m_0) + \gamma m_0 \frac{dv_\phi}{dt} + \gamma m_0 v_r \frac{d\phi}{dt} \right] \\ &\quad + \underline{z} \left[ v_z \frac{d}{dt} (\gamma m_0) + \gamma m_0 \frac{dv_z}{dt} \right] \end{aligned} \quad (3.34)$$

Equating Equation (3.34) to (3.32) and substituting

$$v_r = \dot{r}, \quad v_z = \dot{z} \quad \text{and} \quad v_\phi = r \frac{d\phi}{dt} = r \dot{\phi}$$

gives

$$\frac{d}{dt} (\gamma m_0 \dot{r}) = e \left[ E_r + \mu r H_z \dot{\phi} - \mu H_\phi \dot{z} \right] + \gamma m_0 r \dot{\phi}^2 \quad (3.35)$$

$$\frac{d}{dt} (\gamma m_0 r^2 \dot{\phi}) = e \left[ r E_\phi - \mu r \dot{r} H_z + \mu r H_r \dot{z} \right] \quad (3.36)$$

$$\frac{d}{dt} (\gamma m_0 \dot{z}) = e \left[ E_z + \mu \dot{r} H_\phi - \mu r \dot{\phi} H_r \right] \quad (3.37)$$

Also, since

$$\gamma = \left[ 1 - \frac{\dot{z}^2 + \dot{r}^2 + r^2 \dot{\phi}^2}{c^2} \right]^{-1/2} \quad (3.38)$$

expanding the derivatives and multiplying Equation (3.35) by  $\dot{r}$ , (3.36) by  $\dot{\phi}$  and (3.37) by  $\dot{z}$ , and then adding, leads to

$$\begin{aligned} \dot{\gamma} &= \frac{e}{m_0 c^2} \underline{v} \cdot \underline{E} \\ \therefore \dot{\gamma} &= \frac{e}{m_0 c^2} \left[ \dot{r} E_r + r \dot{\phi} E_\phi + \dot{z} E_z \right] \end{aligned} \quad (3.39)$$

Substituting Equation (3.39) into the expanded derivatives of Equations (3.35), (3.36) and (3.37), and for the  $TM_{010}$ ,  $TM_{110}$  modes letting

$$E_\phi = E_r = H_z = 0$$

gives the following equations (which can be solved numerically):

$$\ddot{r} = r \dot{\phi}^2 + \frac{e}{m_0 \gamma} \left[ -\mu H_\phi - E_z \frac{\dot{r}}{c} \right] \dot{z} \quad (3.40)$$

$$\ddot{\phi} = \frac{e}{r m_0 \gamma} \left[ \mu H_r - \frac{r}{c^2} E_z \dot{\phi} \right] \dot{z} - \frac{2\dot{r}\dot{\phi}}{r} \quad (3.41)$$

$$\ddot{z} = \frac{e}{m_0 \gamma} \left[ E_z + \mu H_\phi \dot{r} - \mu H_r \dot{\phi} - \frac{\dot{z}^2}{c^2} E_z \right] \quad (3.42)$$

$$\dot{\gamma} = \frac{e}{m_0 c^2} E_z \dot{z} \quad (3.43)$$

In rectangular cartesian co-ordinates

$$\underline{v} \times \underline{\mu H} = \mu \begin{vmatrix} \underline{x} & \underline{y} & \underline{z} \\ v_x & v_y & v_z \\ H_x & H_y & H_z \end{vmatrix}$$

$$= \mu \underline{x}(v_y H_z - v_z H_y) + \mu \underline{y}(v_z H_x - v_x H_z) + \mu \underline{z}(v_x H_y - v_y H_x)$$

and Equation (3.31) can be written

$$\frac{d}{dt} (\gamma m_0 v_x) = e \left[ E_x + \mu (v_y H_z - v_z H_y) \right] \quad (3.44)$$

$$\frac{d}{dt} (\gamma m_0 v_y) = e \left[ E_y + \mu (v_z H_x - v_x H_z) \right] \quad (3.45)$$

$$\frac{d}{dt} (\gamma m_0 v_z) = e \left[ E_z + \mu (v_x H_y - v_y H_x) \right] \quad (3.46)$$

For the TE<sub>101</sub>, TE<sub>102</sub> modes,

$$E_x = E_z = H_y = 0$$

and letting

$$v_x = \dot{x}, \quad v_y = \dot{y} \quad \text{and} \quad v_z = \dot{z}$$

the Equations (3.44), (3.45), and (3.46) can be written

$$\gamma \dot{x} + \dot{x} \dot{\gamma} = \frac{e}{m_0} \mu \dot{y} H_z \quad (3.47)$$

$$\gamma \dot{y} + \dot{y} \dot{\gamma} = \frac{e}{m_0} \left[ E_y + \mu (\dot{z} H_x - \dot{x} H_z) \right] \quad (3.48)$$

$$\gamma \dot{z} + \dot{z} \dot{\gamma} = -\frac{e}{m_0} \mu \dot{y} H_x \quad (3.49)$$

Also, since

$$\gamma = \left[ 1 - \frac{\dot{x}^2 + \dot{y}^2 + \dot{z}^2}{c^2} \right]^{-1/2}$$

$$\dot{\gamma} = \frac{e}{m_0 c^2} \dot{y} E_y \quad (3.50)$$

and the above equations become

$$\dot{x} = \frac{e \dot{y}}{m_0 \gamma} \left[ \mu H_z - \frac{\dot{x}}{c^2} E_y \right] \quad (3.51)$$

$$\dot{y} = \frac{e}{m_0 \gamma} \left[ -\mu \dot{x} H_z + \mu \dot{z} H_x + \left( 1 - \frac{\dot{y}^2}{c^2} \right) E_y \right] \quad (3.52)$$

$$\dot{z} = \frac{e \dot{y}}{m_0 \gamma} \left[ -\mu H_x - \frac{\dot{z}}{c^2} E_y \right] \quad (3.53)$$

With initial conditions,  $\dot{x}_0, \dot{z}_0, V_0, x_0, y_0, z_0$  and, for example, with a paraxial beam,

$$V_0 \Rightarrow \gamma_0 \quad \gamma_0 \Rightarrow \dot{y}_0$$

the above equations can be solved numerically for a given time dependence of the sinusoidal fields.

**3.2.2 Relationship of Spatial Co-ordinates with R-F Field Time Dependence.** The TE<sub>102</sub> mode will be the only case discussed in this section, but since the relationship is common to all configurations the results can be readily applied to the other modes of interest.

Multiplying the TE<sub>102</sub> field Equations (2.54), (2.55) and (2.56) by a complex time dependence we obtain

$$E_y = \text{Rl} \left( -j \frac{2a\eta}{\lambda_0} H_{oz} \sin \frac{\pi x}{a} \sin \frac{2\pi z}{d} e^{jf(t)} \right)$$

$$= \frac{2a\eta}{\lambda_0} H_{oz} \sin \frac{\pi x}{a} \sin \frac{2\pi z}{d} \sin f(t) \quad (3.54)$$

$$H_z = \text{Rl} \left( H_{oz} \cos \frac{\pi x}{a} \sin \frac{2\pi z}{d} e^{jf(t)} \right)$$

$$= H_{oz} \cos \frac{\pi x}{a} \sin \frac{2\pi z}{d} \cos f(t) \quad (3.55)$$

$$H_x = R \ell \left( -\frac{2a}{d} H_{oz} \sin \frac{\pi x}{a} \cos \frac{2\pi z}{d} e^{j\omega t} \right)$$

$$= -\frac{2a}{d} H_{oz} \sin \frac{\pi x}{a} \cos \frac{2\pi z}{d} \cos \omega t \quad (3.56)$$

Referring to the co-ordinate system shown in Figure 8(b), and defining a positive  $H_x$  deflecting field in the center of the cavity for the first half cycle, then, to satisfy the conditions,

$$H_x > 0 \quad \text{for} \quad \frac{d}{4} < z < \frac{3d}{4}$$

$$H_x < 0 \quad 0 < z < \frac{d}{4}, \quad \frac{3d}{4} < z < d$$

$$x = 0 \quad H_z > 0 \quad 0 < z < \frac{d}{2}$$

$$H_z < 0 \quad \frac{d}{2} < z < d$$

$$x = a \quad H_z < 0 \quad 0 < z < \frac{d}{2}$$

$$H_z > 0 \quad \frac{d}{2} < z < d,$$

$f(t)$  must equal  $\pm (\omega t - \pi/2)$  for  $0 < \omega t < \pi$ , i. e.,

$$H_x = -\frac{2a}{d} H_{oz} \sin \frac{\pi x}{a} \cos \frac{2\pi z}{d} \sin \omega t \quad (3.57)$$

and, choosing the upper sign,

$$E_y = \frac{2a\eta}{\lambda_o} H_{oz} \sin \frac{\pi x}{a} \sin \frac{2\pi z}{d} \sin \left( \omega t - \frac{\pi}{2} \right) \quad (3.58)$$

giving

$$E_y < 0 \quad \text{for} \quad 0 < z < \frac{d}{2} \quad \text{and} \quad 0 < \omega t < \frac{\pi}{2},$$

and

$$E_y > 0 \quad \text{for} \quad \frac{d}{2} < z < d \quad \text{and} \quad 0 < \omega t < \frac{\pi}{2}.$$

### 3.3 Aberration Computations for Large Beam Cross-Sections and Deflections

The results of applying the Section 3.2 equations to TE<sub>101</sub> and TE<sub>102</sub> copper cavities are discussed below. The parameters chosen for these examples were  $\lambda_o = 0.105$  m,  $P_L = 4$  kW,  $S = 0.20$  m, beam diameters of  $0.1\lambda_o$  and  $0.2\lambda_o$ , and beam energies of 70 and 150 keV.

The computations were based on an initially cylindrical beam having negligible space charge; and no allowance was made for field perturbation due to the beam apertures.

#### 3.3.1 Beam Energy and Cross-Section Variations at a Given Drift Distance for TE<sub>102</sub> Mode Deflections.

Figure 18 shows beam cross-section diagrams for several deflection examples and an initially parallel beam of circular cross-section which enters the central region of a TE<sub>102</sub> cavity, directed along the "y" axis (Figure 8b), perpendicular to the  $H_x$  and  $H_y$  fields. The diagrams were constructed with the position of the deflected central ray (No. 1), for each case, normalized to a common point.

The cross-sections marked A show the aberration effects at the end of a 20 cm drift distance for a 70 keV,  $0.2\lambda_o$  diameter beam and "h" dimensions of 1.6 and 2.4 cm. The diagrams marked B compare 70 and 150 keV,  $0.1\lambda_o$  and  $0.2\lambda_o$  diameter beams for a 20 cm drift length and optimum values of "h". The cross-sections A and B are for particles which reach the center of the cavity ( $y = h/2$ ) when the deflecting magnetic field ( $H_x$ ) passes through peak positive and negative values, respectively.

A feature which is common to all cases is an elliptic distortion of the beam cross-section due to a net focusing force in the plane of deflection and a weak defocusing force in the orthogonal plane. Furthermore, it can be noted that the centroid of charge (assuming an initially symmetric radial distribution) has a tendency to migrate outward in the direction of deflection, as indicated by the modified location of the initial vertical central plane shown on the B cross-sections.

The focusing effect and centroid migration, in the direction of deflection, are caused predominately by velocity modulation forces due to  $E_y$  and  $\dot{z}\mu H_x$  variations as integrated over the deflection trajectory of the particle ( $0 \leq y \leq h$ ). The weak defocusing force arises mainly from the off-axis ( $x \neq a/2$ ) cross product component  $\dot{y}\mu H_z$ . The beam energy variations for several of the Figure 18 orbit examples are listed in Table VII together with deflection values based on the theoretical Q.

The Table VII entry angles and transit times correspond to maximum deflection conditions, and the data will, of course, be modified for other times during the r-f cycle. Beam energy information of this nature when integrated over the r-f cycle and combined with the charge distribution enables the beam coupling characteristics of the mode to be evaluated.

#### 3.3.2 TE<sub>101</sub> Mode Beam Deflection Aberration Characteristics.

The TE<sub>101</sub> mode aberration effects for 70 and 150 keV deflected beams of  $0.1$  and  $0.2\lambda_o$  diameter are shown in Figure 19. The initial beam conditions were chosen as in Section 3.3.1, however, in order to take advantage of the peak  $H_z$  deflecting field (see Figure 2(b)), the "y" directed beam was off-set such that the outer periphery (orbit No. 4) was located

close to the side wall. To avoid beam collision with the cavity wall, due to deflections of approximately 2 mm within the cavity, the entry position of the beam was based on entry co-ordinates for orbit No. 4 of  $x_0 = 0.0025$  m and  $z_0 = d/2$  for all examples. In order to illustrate overlap characteristics of the large diameter beam, the deflection cross-section diagrams A, B and C of Figure 19 were constructed directly from the deflection values; and unlike the case of Figure 18 these values were not normalized to a common point.

For entry angles ( $\omega t_0$ ), which produce maximum particle deflection in the -x direction (a peak positive  $H_z$  field when the beam reaches the center of the cavity), the cross-section diagrams marked A show a considerable defocusing especially in the direction of deflection. The B diagrams, corresponding to the "straight ahead" condition with entry phases of ( $\omega t_0 + \pi/2$ ), also exhibit this defocusing characteristic but to a lesser degree.

Unlike A and B, the C diagrams at the other deflection extremity ( $\omega t_0 + \pi$ ) indicate the presence of strong focusing forces in the direction of deflection. The original circular cross-section of  $0.2 \lambda_0$  diameter transforms through an elliptic stage, shown at  $S = 10$  cm, into a grossly distorted profile at  $S = 20$  cm. This effect is due to the relatively large area occupied by the beam within the cavity. The No. 2 orbit being in a low deflecting magnetic field environment gains less than half of the transverse momentum received by the No. 4 orbit. In the case of the 70 keV beam, this difference is sufficient to cause a deflection cross-over prior to traversal of the 20 cm drift distance. The wide spread in emergent energy, caused by large electric field gradients due to the off-set beam geometry, also contributes to the profile distortion.

Beam energy and deflection values for several of the Figure 19 beam cross-section examples are listed in Table VIII for different times during the r-f cycle.

As predicted by the Table V data, the TE<sub>101</sub> mode compares very unfavorably with the TE<sub>102</sub> mode for deflection of large diameter beams. The Figure 19  $0.2 \lambda_0$  beam diameter examples show that at one extremity of the sweep ( $\omega t_0$ ) even though the No. 4 orbit deflection is much greater than the entry beam diameter the resulting defocusing is sufficient to cause overlap with the straight ahead beam position ( $\omega t_0 + \pi/2$ ). At  $S = 20$  cm an initial 2.1 cm diameter spreads to 4.63 and 4.20 cm in the direction of deflection for 70 and 150 keV beams, respectively. Even though the deflected beam charge density is considerably reduced in the overlap region, as indicated by the displacement of the centroid plane, aberration of this type would be unacceptable for applications which require complete cut-off. On the other hand, at the other deflection extremity ( $\omega t_0 + \pi$ ) the strong r-f focusing and velocity modulation characteristics may well be exploited (within the bounds of space charge) by incorporation of the cavity in an appropriate system.

3.3.3 TE<sub>101</sub> and TE<sub>102</sub> Beam Loading Characteristics During Deflection. Values of emergent beam total energy at various times during the r-f cycle for the TE<sub>101</sub> and TE<sub>102</sub> cavity examples of Figures 19 and 18 are listed in Tables IX and X, respectively. The listed values (applicable to 70 keV entry energy) indicate the manner in which energy is transferred between the r-f fields and the various beam trajectories. Thus, by appropriately weighting the orbital data in accordance with a given cross-sectional charge distribution, it is possible to determine the beam loading characteristics of the system.

The apparent net increase in beam energy for these examples suggests positive beam loading conditions and supports the theory that beam induced deflection fields can be readily established under bunched beam conditions. This is of particular interest when considering the TEM<sub>11</sub> pulse break-up mode in linear accelerator structures; and the above technique provides a means of studying the starting-up and energy transfer mechanisms for this phenomenon. This is especially applicable to the case of band edge interaction\* where the  $v_p = c$  line intersects higher pass band  $\omega - \beta$  curves in close proximity to the zero group velocity cut-off point ( $\beta d = \pi$ ). Under these conditions small transverse deflection fields can be produced by the beam in individual cavities within a waveguide section; as distinct from the regenerative backward wave mechanism. Short interval steps in azimuthal rotation of the deformation plane (tuning plungers) during waveguide tuning, as performed on some high current and long waveguide designs, will tend to avoid mode polarization and prevent this transverse disturbance from coherently coupling to the beam within subsequently located identical design sections. More powerful suppression techniques include (a) differential absorption of the higher order modes by internal loading or coupling into external loads and (b) the use of structures which possess higher order mode split pass-band characteristics in the vicinity of the  $v_p = c$  intercept.

### 3.4 Some Selected Examples of Transverse Magnetic Deflection Cavities

A detailed discussion relating to applications of the cavities presented in this section may be found elsewhere.<sup>2</sup> Figure 20 shows a typical TE<sub>102</sub> S-band chopper cavity and gun anode assembly for an injector chopper-prebuncher system. A loaded Q of 800 (with critical coupling) was obtained with this cavity by using non-magnetic steel for five of the wall surfaces and OFHC copper (anode plate) for the other. The cooling tubes, r-f input coupler and tuner (bellows) are clearly indicated. Water jets for anode cooling and magnet pole pieces for d-c-biasing of the beam are located in the apertures around the periphery of the anode plate.

Figure 21(a) shows two end caps and an integral block assembly which contains two TE<sub>102</sub> cavities oriented at right angles to each other. The patterns on the inner surfaces are multipactor suppression grooves. The

tungsten screen beam traces depicted in Figure 21(b) were obtained by driving these cavities in phase quadrature to provide (a) r-f rotation of a transmitted 120 keV, 3A unchopped beam and (b) bunch monitoring of the beam after being subjected to progressively increased chopping action produced by a separate TE<sub>102</sub> cavity similar to that shown in Figure 20.

Figure 22 shows a 476 MHz, TE<sub>101</sub> chopper cavity for 1 bunch in 6 selection as used in the injection system of a 2856 MHz linear accelerator for synchrotron injection. The beam aperture, located in a region of maximum transverse magnetic field, can be noted at the periphery of the cavity.

The author wishes to thank his colleagues for their encouragement and support during the course of these projects and Varian Associates for permission to present this material.

References

1. J. Haimson, IRE Trans. Nucl. Sci. 9, 32 (1962).
2. J. Haimson, Varian Report TMO-90 (Feb. 1966).
3. W. K. H. Panofsky and W. A. Wenzel, Rev. Sci. Inst. 27, 967, (1956).
4. Fields and Waves in Modern Radio, S. Ramo and J. R. Whinnery, (1953).
5. Radiation Laboratory Series No. 11, Ed., C. G. Montgomery, (1947).
6. J. Haimson, Nucl. Instr. Meth., 33, 93 (1965).

-----  
\*Refer IEEE, Trans. Nucl. Sci. Vol. NS-12, Page 997, June 1965.

TABLE I  
COMPARISON OF OPTIMIZED H FIELD MAXIMA  
FOR THE TM<sub>010</sub> AND TE<sub>101</sub> MODES

$\frac{h}{\lambda_o}$	TM <sub>010</sub>		TE <sub>101</sub>				
	$\frac{a}{\lambda_o}$	$H_{\phi M} \lambda_o \sqrt{\frac{R_s}{P_L}}$	$\frac{a}{d}$	$\frac{a}{\lambda_o}$	$\frac{d}{\lambda_o}$	$H_z M \lambda_o \sqrt{\frac{R_s}{P_L}}$	$H_x M \lambda_o \sqrt{\frac{R_s}{P_L}}$
.152	.383	1.397	0.609	.585	.961	1.881	1.145
.329	.383	1.212	0.626	.590	.942	1.609	1.008
.429	.383	1.135	0.632	.592	.936	1.499	0.948
.152			1.000	.707	.707	1.672	1.672
.329			1.000	.707	.707	1.440	1.440
.429			1.000	.707	.707	1.345	1.345

TABLE II  
COMPARISON OF Q VALUES FOR THE TM<sub>010</sub> AND TE<sub>101</sub> MODES

$\frac{h}{\lambda_o}$	Q <sub>R<sub>s</sub></sub>		Q in copper at f = 2856 MHz	
	TM <sub>010</sub>	Optimum TE <sub>101</sub>	TM <sub>010</sub>	Optimum TE <sub>101</sub>
0.152	129.0	123.1	9250	8825
0.329	209.5	195.0	15000	14000
0.429	239.5	221.0	17160	15800

TABLE IV  
COMPARISON OF Q VALUES FOR THE TM<sub>110</sub> AND TE<sub>102</sub> MODES

$\frac{h}{\lambda_0}$	QR <sub>s</sub>				Q in copper at 2856 MHz			
	TM <sub>110</sub>		Optimum TE <sub>102</sub>		Optimum TE <sub>102</sub>		Optimum TE <sub>102</sub>	
	H <sub>ZM</sub>	H <sub>XM</sub>	H <sub>ZM</sub>	H <sub>XM</sub>	H <sub>ZM</sub>	H <sub>XM</sub>	H <sub>ZM</sub>	H <sub>XM</sub>
0.152	144.3	127.5	141.7	10340	9140	10160	17540	20560
0.329	252.8	208.8	244.7	18120	14970	17540	20560	20560
0.429	298.1	240.1	286.8	21370	17210	20560	20560	20560

TABLE V  
PERCENTAGE (BIN) VARIATION OF H FIELD ACROSS THE BEAM DIAMETER IN THE DIRECTION OF DEFLECTION

Beam Diameter	TM <sub>010</sub> H <sub>φM(r)</sub> *	TE <sub>101</sub> H <sub>ZM(x)</sub>	TE <sub>101</sub> (a = d) H <sub>Z = H<sub>x</sub></sub>	TM <sub>110</sub> H <sub>φM(r)</sub> *	TE <sub>102</sub> H <sub>ZM(x)</sub>	TE <sub>102</sub> H <sub>XM(z)</sub> *
0.05λ <sub>0</sub>	0.8	2.8	2.7	1.0	3.7	1.2
0.10λ <sub>0</sub>	3.2	12.5	10.0	3.5	13.3	4.0
0.15λ <sub>0</sub>	7.3	28.0	21.8	8.0	28.4	8.4
0.20λ <sub>0</sub>	17.0	49.0	37.4	14.5	49.2	14.8
Relative H = Maxima	0.753	1.000	0.895	0.814	0.727	0.794

\* Symmetric H field distribution about the beam center-line.

TABLE III  
COMPARISON OF OPTIMIZED H FIELD MAXIMA FOR THE TM<sub>110</sub> AND TE<sub>102</sub> MODES

$\frac{h}{\lambda_0}$	TM <sub>110</sub>				TE <sub>102</sub>			
	$\frac{a}{\lambda_0}$	$H_{\phi M} \lambda_0 \sqrt{\frac{R_s}{P L}}$	$\frac{a}{d}$	$\frac{d}{\lambda_0}$	$H_{ZM} \lambda_0 \sqrt{\frac{R_s}{P L}}$	$\frac{d}{\lambda_0}$	$H_{XM} \lambda_0 \sqrt{\frac{R_s}{P L}}$	$\frac{d}{\lambda_0}$
0.152	0.610	1.453*	0.315	1.876	1.351*	1.876	0.851	1.876
0.329	0.610	1.310*	0.337	1.789	1.170*	1.789	0.788	1.789
0.429	0.610	1.245*	0.344	1.763	1.095*	1.763	0.754	1.763
0.152			0.875	1.007	1.152	1.007	1.428*	1.007
0.329			0.881	1.013	1.150	1.013	1.278*	1.013
0.429			0.883	1.015	1.149	1.015	1.211*	1.015
0.152			0.500	0.707	1.230	0.707	1.230	0.707
0.329			0.500	0.707	1.086	0.707	1.086	0.707
0.429			0.500	0.707	1.024	0.707	1.024	0.707

\* Maximized values

TABLE VI  
COMPARISON OF OPTIMIZED E FIELD MAXIMA

$\frac{h}{\lambda_0}$	$E_{zM} \frac{\sqrt{R}}{\eta} \sqrt{\frac{P}{L}}$		$E_{yM} \frac{\sqrt{R}}{\eta} \sqrt{\frac{P}{L}}$	
	TM <sub>010</sub>	TM <sub>110</sub>	TE <sub>101</sub> for H <sub>zM</sub>	TE <sub>102</sub> for H <sub>xM</sub>
0.152	2.401	1.691	2.202	1.645
0.329	2.083	1.524	1.899	1.470
0.429	1.950	1.449	1.774	1.392

TABLE VII  
COMPARISON OF TE<sub>102</sub> MODE DEFLECTION AND BEAM ENERGY FOR VARIOUS BEAM POSITIONS

Entry Angle ( $\omega_0^0$ )	Electron Beam Parameters	Figure 18		Total Energy (keV) at		Energy (keV) Corresponding to $\dot{y}$	Beam Position After Deflection at S = 20 cm z (cm)
		Orbit No.	$z_0$ (cm)	$y = \frac{h}{2}$	$y = h$		
3.3	V <sub>0</sub> = 70 keV dia = 0.1λ <sub>0</sub>	1	6.04	69.95	71.36	69.48	9.21
		11	6.57	64.01	71.86	70.22	9.51
		13	5.52	76.11	71.56	69.69	8.65
4.0	V <sub>0</sub> = 70 keV dia = 0.2λ <sub>0</sub>	2	6.04	69.95	71.24	69.52	9.05
		4	7.09	58.71	72.90	71.70	9.59
		6	6.04	69.95	71.24	69.52	9.05
		8	4.99	82.01	72.36	70.81	7.81
4.0	V <sub>0</sub> = 150 keV dia = 0.1λ <sub>0</sub>	1	6.04	149.93	151.94	148.47	8.74
		11	6.56	142.39	152.29	149.19	9.12
		13	5.51	157.61	151.84	148.50	8.16
4.0	V <sub>0</sub> = 150 keV dia = 0.2λ <sub>0</sub>	2	6.04	149.93	151.76	148.60	8.82
		4	7.09	135.54	152.83	150.48	9.31
		6	6.04	149.93	151.76	148.60	8.62
		8	4.99	164.84	151.99	149.26	7.37
183.3	V <sub>0</sub> = 70 keV dia = 0.1λ <sub>0</sub>	1	6.04	69.95	71.36	69.48	2.88
		11	6.57	76.11	71.56	69.69	3.44
		13	5.52	64.01	71.86	70.22	2.58

Cavity dimensions, a = 0.1062 m, d = 0.1208 m and h = 0.0241 m for the 70 keV examples, and a = 0.1064 m, d = 0.1207 m and h = 0.032 m for the 150 keV examples.

TABLE VIII  
COMPARISON OF TE<sub>101</sub> MODE DEFLECTION AND BEAM ENERGY FOR VARIOUS BEAM POSITIONS

Entry Angle ( $\omega_0^0$ )	Electron Beam Parameters	Figure 19		Total Energy (keV) at		Energy (keV) Corresponding to $\dot{y}$	Beam Position After Deflection at S = 20 cm x (cm)
		Orbit No.	$x_0$ (cm)	$y = \frac{h}{2}$	$y = h$		
8.2	V <sub>0</sub> = 70 keV dia = 0.1λ <sub>0</sub>	4	0.25	73.38	71.92	68.75	-3.87
		8	0.77	80.47	71.85	68.98	-3.12
		1	1.30	87.33	72.70	70.43	-2.12
		7	0.77	80.47	71.85	68.98	-3.12
		6	0.77	80.62	71.91	68.97	-3.17
		5	1.30	86.36	72.35	70.31	-1.93
8.5	V <sub>0</sub> = 70 keV dia = 0.2λ <sub>0</sub>	2	2.35	96.91	75.04	74.51	0.76
		3	1.30	86.36	72.38	70.31	-1.93
		4	0.25	154.18	152.62	147.04	-3.19
8.5	V <sub>0</sub> = 150 keV dia = 0.1λ <sub>0</sub>	8	0.77	162.85	152.03	147.11	-2.44
		1	1.30	171.09	151.92	148.08	-1.53
		7	0.77	162.85	152.03	147.11	-2.44
		6	0.77	163.03	152.09	147.04	-2.49
		5	1.30	169.91	151.68	148.18	-1.37
		2	2.35	182.42	152.19	151.30	1.01
98.2	V <sub>0</sub> = 70 keV dia = 0.2λ <sub>0</sub>	3	1.30	169.91	151.68	148.18	-1.37
		4	0.25	66.36	64.08	64.07	0.39
		5	1.30	51.22	39.57	39.54	1.77
98.5	V <sub>0</sub> = 150 keV dia = 0.2λ <sub>0</sub>	2	2.35	39.42	29.24	29.22	2.72
		1	1.30	50.16	38.28	38.24	1.83
		4	0.25	145.52	142.73	142.72	0.27
		5	1.30	126.78	108.35	108.32	1.46
188.5	V <sub>0</sub> = 150 keV dia = 0.2λ <sub>0</sub>	2	2.35	112.13	84.78	84.77	2.51
		1	1.30	125.44	106.17	106.14	1.49
		4	0.25	145.64	153.47	148.12	3.61
		5	1.30	130.82	155.45	152.53	3.72
		2	2.35	119.76	158.11	157.46	3.49
		1	1.30	129.73	155.95	152.81	3.84

Cavity dimensions, a = 0.0617 m, d = 0.10 m and h = 0.023 m for the 70 keV examples, and a = 0.0619 m, d = 0.0992 m and h = 0.0309 m for the 150 keV examples.

TABLE IX

VARIATION OF BEAM ENERGY WITH TIME DURING THE R-F CYCLE FOR THE  $TE_{101}$  MODE

Entry Angle	Figure 19 Total Beam Energy (keV)				
	Orbit No. 1	2	3	4	5
$\omega t_0$	72.70	75.04	72.38	71.92	72.38
$\omega t_0 + \pi/2$	38.28	29.24	39.57	64.08	39.57
$\omega t_0 + \pi$	77.01	81.29	76.38	72.84	76.38
$\omega t_0 + 3\pi/2$	112.76	134.53	110.30	80.07	110.30

TABLE X

VARIATION OF BEAM ENERGY WITH TIME DURING THE R-F CYCLE FOR THE  $TE_{102}$  MODE

Beam Diameter	Entry Angle	Figure 18 Total Beam Energy (keV)								
		Orbit No. 1	2	4	6	8	10	11	12	13
$.1\lambda_0$	$\omega t_0$	71.36	71.33	71.86	71.33	71.56	71.33	71.33	71.33	71.56
	$\omega t_0 + \pi/2$	71.35	71.31	84.52	71.31	58.85	71.31	71.31	71.31	58.85
	$\omega t_0 + \pi$	71.36	71.33	71.56	71.33	71.86	71.33	71.33	71.33	71.86
	$\omega t_0 + 3\pi/2$	71.35	71.31	58.85	71.31	84.52	71.31	71.31	71.31	84.52
$.2\lambda_0$	$\omega t_0$	71.36	71.24	72.90	71.24	72.36	71.24	71.24	71.24	72.36
	$\omega t_0 + \pi/2$	71.35	71.22	97.09	71.22	48.24	71.22	71.22	71.22	48.24
	$\omega t_0 + \pi$	71.36	71.24	72.36	71.24	72.90	71.24	71.24	71.24	72.90
	$\omega t_0 + 3\pi/2$	71.35	71.22	48.24	71.22	97.09	71.22	71.22	71.22	97.09

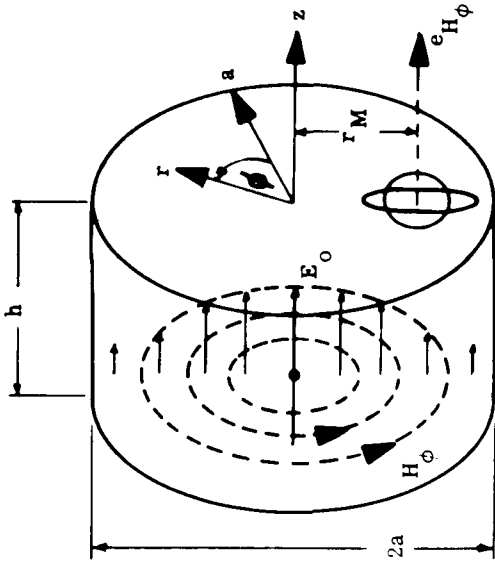


Fig. 1(a) Circular cylindrical cavity  $TM_{010}$  mode.

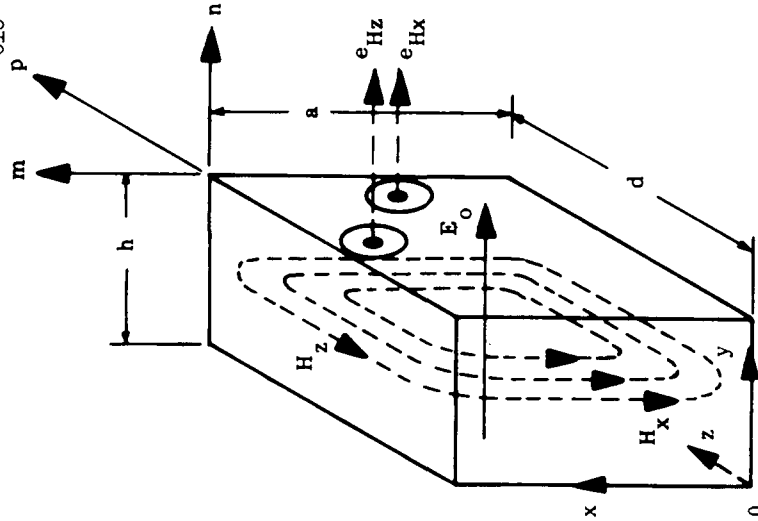


Fig. 1(b) Rectangular waveguide cavity  $TE_{101}$  mode.

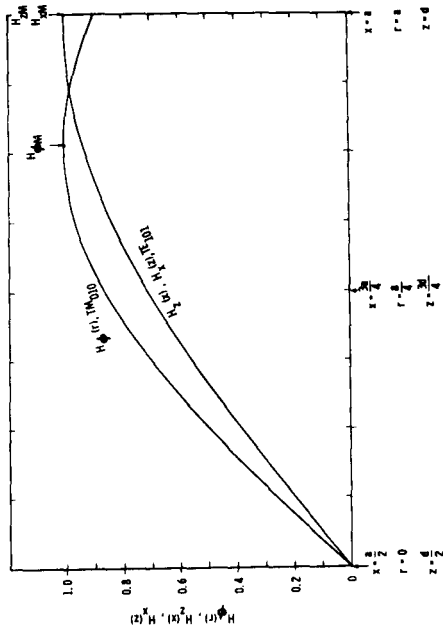


Fig. 2. Magnetic field distributions  $H_x(x)$  and  $H_z(z)$ .

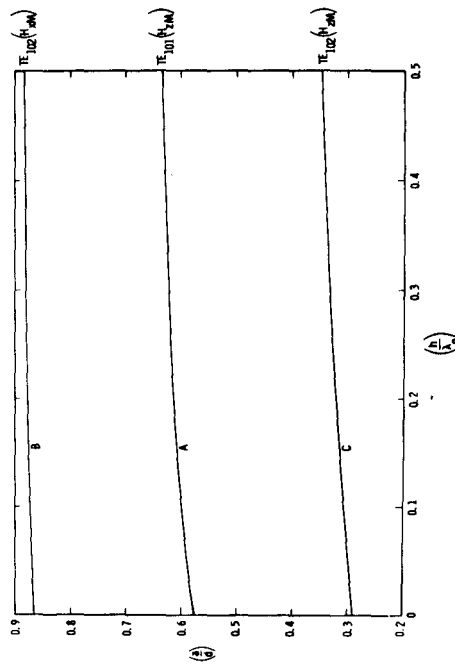


Fig. 3. Optimum  $(a/d)$  ratio versus  $(h/\lambda_0)$  for  $TE_{101}$  and  $TE_{102}$  modes.

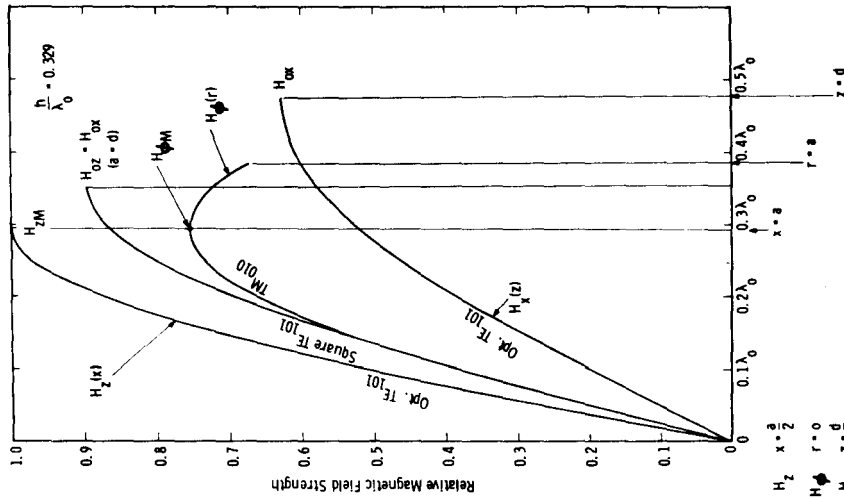


Fig. 4. Comparison of magnetic field gradients in the direction of beam deflection for  $TM_{010}$  and  $TE_{101}$  modes.

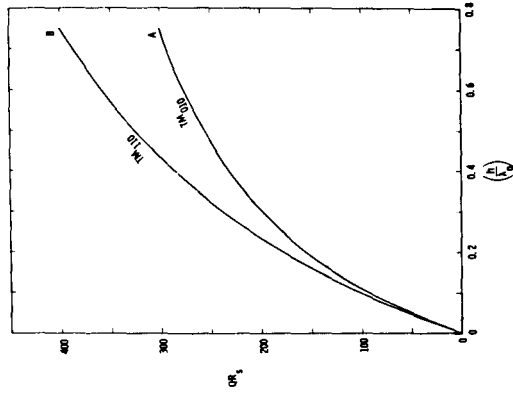


Fig. 5. Variation of  $QR_s$  with  $(h/\lambda_0)$  for the  $TM_{010}$  and  $TM_{110}$  modes.

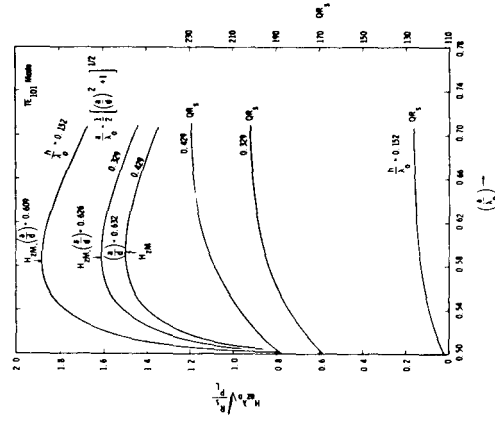


Fig. 6. Variation of  $AR_s$  and peak magnetic field with  $(a/\lambda_0)$  for the  $TE_{101}$  mode.

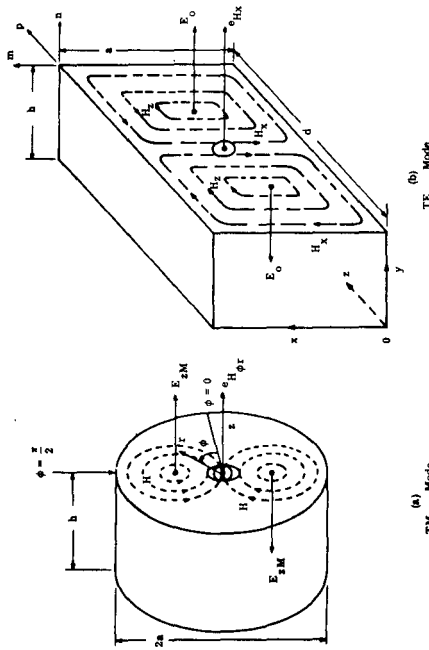


Fig. 8.  $TM_{110}$  and  $TE_{102}$  mode field patterns.

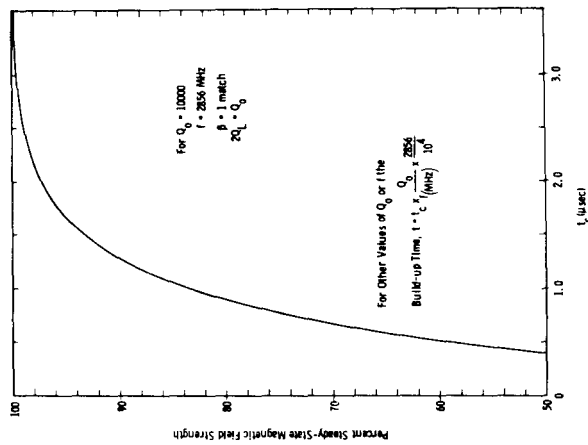


Fig. 7. Magnetic field strength build-up time characteristic.

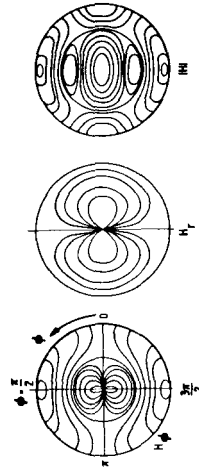


Fig. 9.  $TM_{110}$  magnetic field distributions  $H_r(r)$  in the  $\phi = 0$  plane and  $H_\phi(r)$  in the  $\phi = \pi/2$  plane.

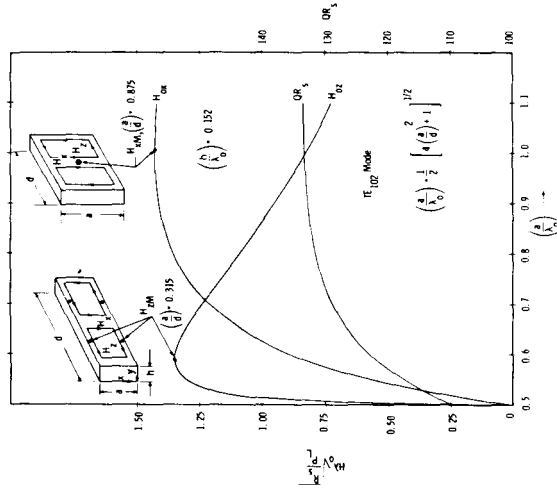


Fig. 10. Variation of  $QR$  and peak magnetic fields with  $(a/\lambda_0)$  for the  $TE_{102}$  mode and  $(b/\lambda_0) = 0.152$ .

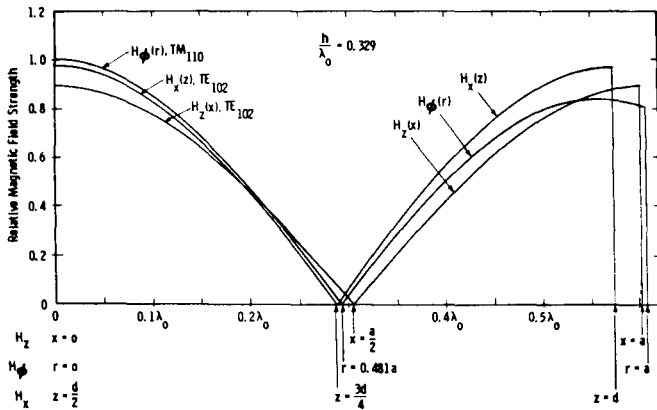


Fig. 11. Gradients of optimized magnetic fields in the direction of beam deflection for  $TM_{110}$  and  $TE_{102}$  modes.

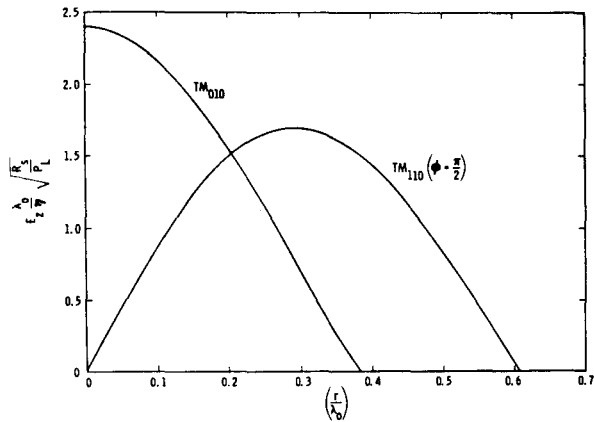


Fig. 13. Radial dependence of longitudinal electric field ( $E_z$ ) for the  $TM_{010}$  and  $TM_{110}$  modes.

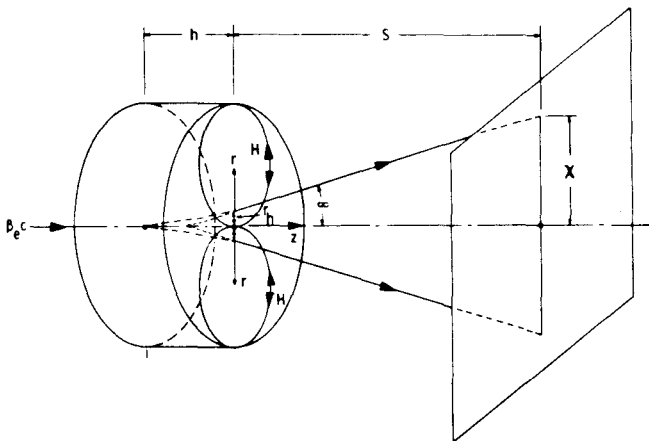


Fig. 14.  $TM_{110}$  cavity and beam deflection paths.

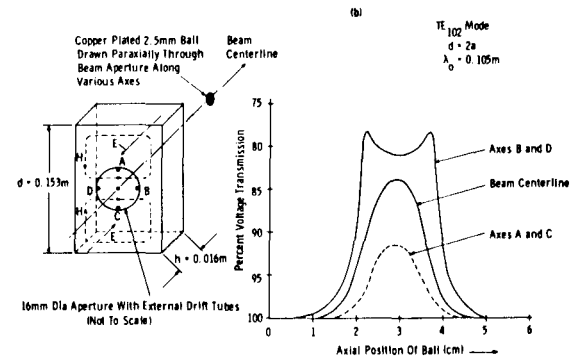
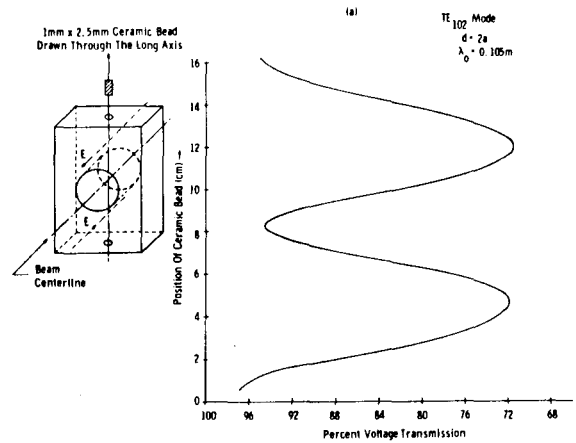


Fig. 12.  $TE_{102}$  cavity bead perturbation experimental data.

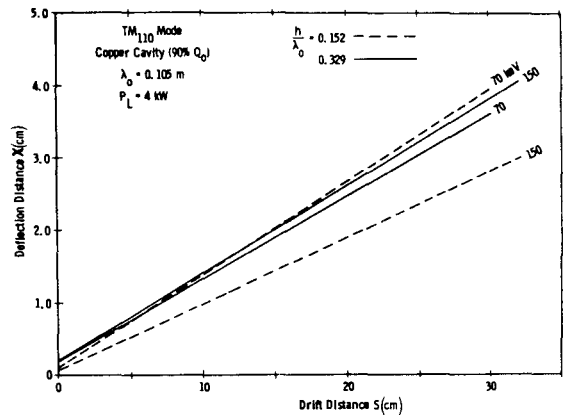


Fig. 15.  $TM_{110}$  cavity beam deflection versus drift length.

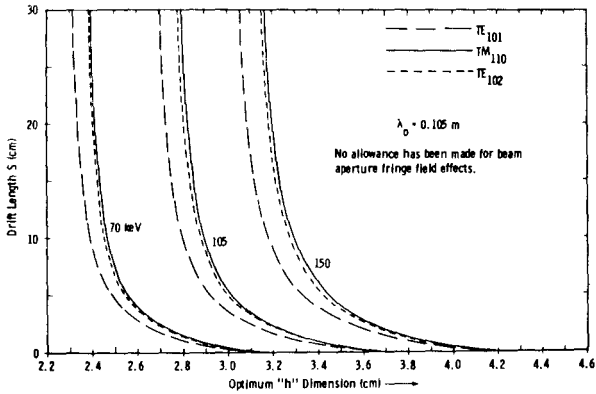


Fig. 16.  $TM_{110}$ ,  $TE_{101}$  and  $TE_{102}$  optimum "h" dimension versus drift length for various beam energies at 2856 MHz.

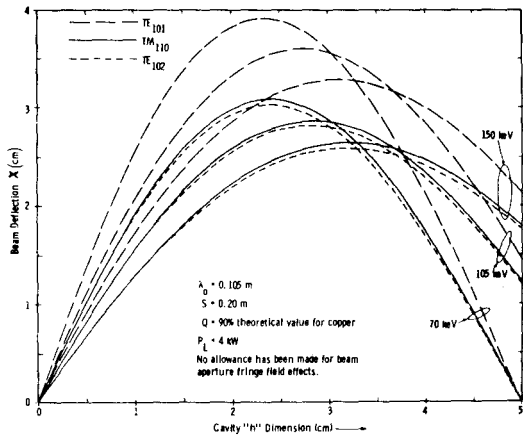


Fig. 17. Beam deflection versus "h" dimension for a given drift length and input R-F power and various beam energies.

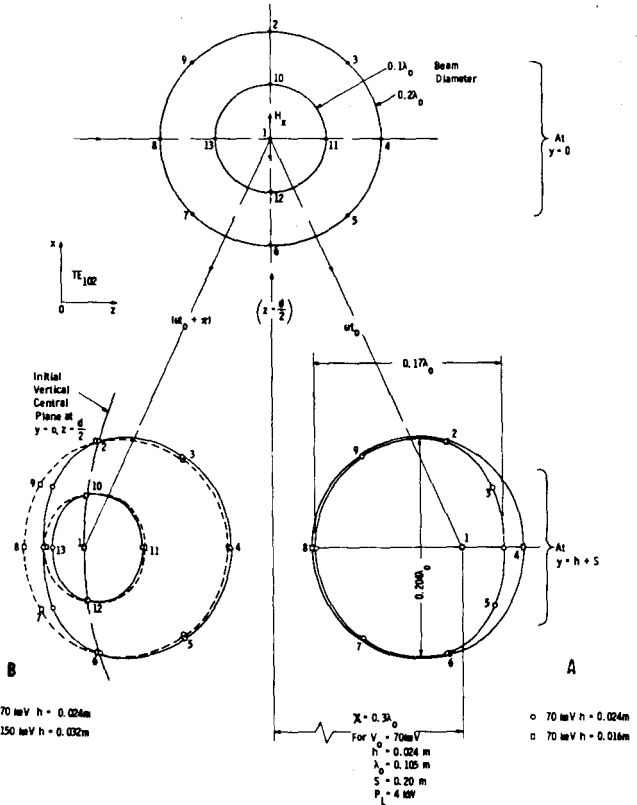


Fig. 18. Beam cross-section variations for  $TE_{102}$  cavity deflections.

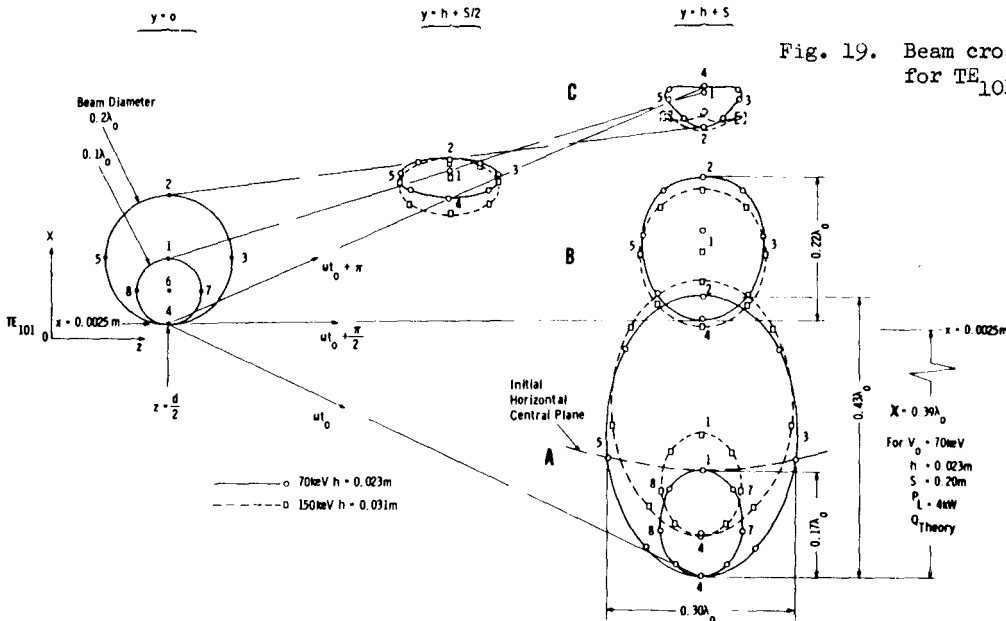


Fig. 19. Beam cross-section variations for  $TE_{101}$  cavity deflections.

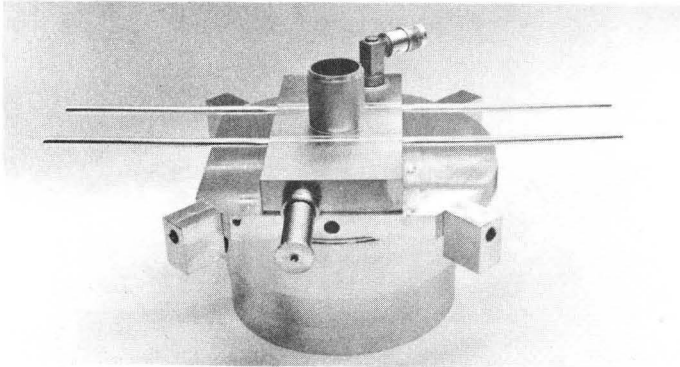


Fig. 20. Electron gun anode and chopper cavity assembly during construction.

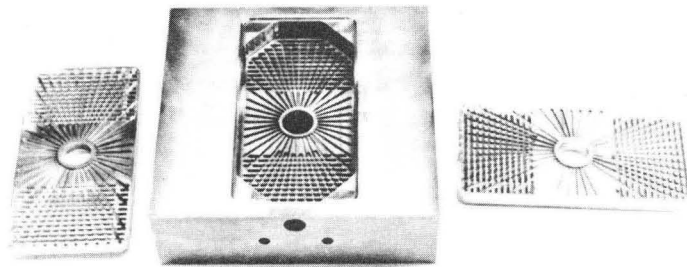


Fig. 21a. Transverse deflection higher order mode dual cavity assembly for beam rotation and monitoring of R-F bunch length.

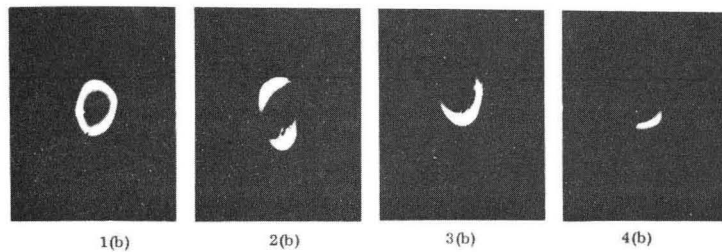


Fig. 21b. Tungsten screen photographs showing beam rotation and R-F chopping at S-band frequency.

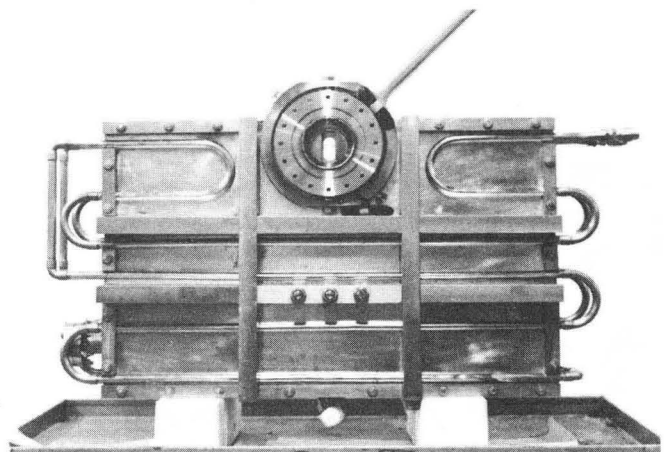


Fig. 22. 476 MHz,  $TE_{101}$  transverse magnetic chopper cavity for one in six bunch selection.